EXPLORATION OF CRYSTALLOGRAPHIC DEFECTS IN TOPOLOGICAL INSULATOR METAMATERIALS

BY

SASHA SENECA YAMADA

THESIS

Submitted in partial fulfillment of the requirements
for the degree of Master of Science in Electrical Engineering
in the Graduate College of the
University of Illinois Urbana-Champaign, 2021

Urbana, Illinois

Adviser:

Professor Gaurav Bahl

ABSTRACT

Topological phases of matter have attracted the interest of physicists and engineers due to their novel transport properties and ability to protect robust states at material boundaries. These phases of matter occur when symmetries quantize and protect an invariant material property [1]. While initially thought to be unusual behavior, computational analysis of stoichiometric materials has revealed that over 27% of all materials in nature are topologically non-trivial [2]. The prevalence of these materials provides further cause to study their behavior; however, it remains an experimental challenge to exercise precise control of materials at an atomic level. Fortunately, the topological properties of these materials are governed by the wave-nature of electrons which allows classical analogues to be constructed from metamaterials. Such metamaterials have been constructed using mechanical [3, 4, 5, 6], electronic [7, 8], and photonic [9, 10] platforms to study topological phenomena. This thesis describes the construction of circuit-based resonator arrays and their application to experimentally investigate how crystallographic defects interact with a material's topology. Specifically, partial dislocation defects in multipole topological insulators are considered. It is observed that these defects can trap robust bound states at their defect core, which provides a pathway to embed protected topological states deep within the bulk of a material.

To Brett, and our cats Mochi & Kalo

ACKNOWLEDGMENTS

I would firstly like to thank Professor Gaurav Bahl for his guidance while pursuing these research topics. He has challenged me to evaluate my work from a different perspective, and for that, I am grateful. I would also like to thank Professor Taylor Hughes and his students for the helpful discussions about topological physics. I am additionally appreciative of Professor Jennifer Bernhard, and would like to thank her for her support and advice.

I am grateful for the financial support of the National Science Foundation as a Graduate Research Fellow (Grant No. DGE – 1746047) and to Professors Wayne Shiroma and Aaron Ohta at the University of Hawaiʻi at Mānoa for encouraging me to apply for this award.

To my lab mates in the Bahl group, thank you for your camaraderie over the past two years. I have enjoyed getting to know each one of you as both colleagues and friends.

To my friends and family, thank you for supporting my ambitions—even when they have led me to live 4,000 miles away, surrounded by cornfields.

Finally, to my wonderful fiancé, Brett, my sincerest thanks. I would not be where I am today, or who I am today, without his love and support.

TABLE OF CONTENTS

CHAPTER 1

INTRODUCTION

This chapter provides context for the work presented in this thesis by introducing the concepts of topology and topological insulators. These topics are first explained with respect to their historical origin in Section 1.1.1. Next, a simple model of a 1D topological insulator is introduced and the principal physics of these materials are discussed in Section 1.1.2. This is followed by a brief introduction to quantized electric multipole insulators in Section 1.1.3. Finally, the motivation for this work and how it relates to engineering is presented in Section 1.2. This work was first published in S. S. Yamada et al. [11] and is adapted here with permission.

1.1 Topology & topological insulators

This section provides a brief introduction to topological insulators by discussing the historical origins of the field and introducing a few simple models.

1.1.1 Historical origins

Topology has its origins in mathematics and is a field concerned with characterizing properties of a system that are conserved under continuous deformation [1, 12]. One of the most common examples used to describe topology is the claim that a coffee mug and a doughnut are topologically equivalent surfaces (Fig. 1.1). To support this claim, one must identify a property that does not change under continuous deformation—this property is known as the topological invariant. In the coffee mug example, the topological invariant is the number of holes through a surface, known as the "genus." By this definition, the genus of a surface must be an integer-valued quantity. Fig. 1.1 illustrates two sets of topologically equivalent surfaces of different genus. Surfaces of the same genus can be continuously deformed into one another and thus are topologically equivalent. Surfaces of different genus cannot be deformed into one another without using discontinuous deformations (e.g., cutting, gluing). Hence, surfaces of different genus are topologically distinct.

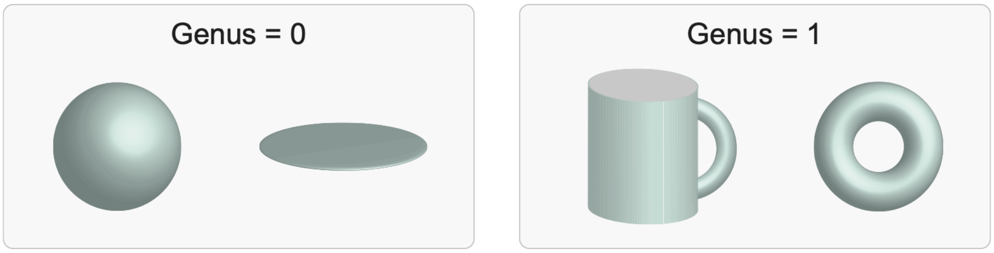

Figure 1.1: Depiction of topologically equivalent surfaces. Here, the topological invariant (genus) is defined to be the number of holes through an otherwise continuous surface.

These seemingly abstract concepts of topology have proven to be instrumental in understanding material properties like conductance and magnetism at a quantum level. In the early 1970s, two physicists at the University of Birmingham, David Thouless and Michael Kosterlitz, discovered that topological phase transitions occur in 2D materials [13]. Their discovery, now known as the KT transition (Kosterlitz-Thouless transition), challenged the prevailing belief at the time, which was that thermal fluctuations would prohibit the formation of any ordered phases in 2D matter [13]. What they found instead, was that ordered phases not only occurred, but had distinct topological features that evolved with increasing temperature [13]. This discovery explained why superconductivity/superfluidity occurred at low temperatures and disappeared at higher temperatures. The KT-transition is particularly useful because it is a general theory which can be applied to explain unusual physics in other low-dimensional materials. The KT-transition has since been recognized as one of the most important discoveries of the 20th century [13] and was a precursor to some of the most exciting breakthroughs in condensed matter physics in this century.

Further advances in experimental research eventually led to the discovery of the integer quantum Hall effect by Klaus von Klitzing in 1980 [14]. His experiment concerned the 2D interface between two semiconductors, cooled to a few degrees Kelvin and subjected to a strong magnetic field [13]. Strikingly, he observed that the electrical conductance changed in a step-wise manner when he swept the magnetic field strength. This observation was remarkable because of how precisely the conductivity was quantized, leading physicists to wonder what was responsible for this effect [14]. Several years later, David Thouless and Duncan Haldane had independently converged at a possible answer: topology [13].

Specifically, it was the topology of the Berry phase that this quantization could be attributed to [1]. The Berry phase is the phase accumulated by each electron as it traverses a closed path in momentum-space ("k"-space) [1]. Computing the Berry phase acquired over the Brillouin zone of a 2D material for a single energy band results in an integer-valued quantity called the Chern number [1, 12]. This quantity is the topological invariant responsible for the integer quantum Hall effect [1]. If the Chern number of a given energy band is non-zero, the material is topologically non-trivial over that range of energy and will exhibit spectrally gapless (i.e., conductive) unidirectional propagating modes localized at the material boundaries [1, 12]. These modes are considered to be "protected" because they are robust to any material defects and deformations that do not cause the topological invariant to change. For topological insulators, which are materials that have insulating bulk band structure but can host topologically protected modes at the material boundaries, changes of the topological invariant are necessarily associated with the closing of the bulk band gap [12]. Since the spectrally gapless boundary modes are a manifestation of a material's non-trivial topology, they are guaranteed to exist so long as the bulk band gap does not close.

While the discussion above focuses on electronic materials, analogous topological behavior has been demonstrated in a wide variety of physical systems. This is due to the topological physics being a result of the wave-like nature of electrons, rather than a strictly quantum effect [1, 12]. Notably, mechanical [3, 4, 5, 6], electronic [8], and photonic [15, 9, 10] metamaterials have been used to construct topological insulator models; this approach has rapidly accelerated experimental research in this field. Furthermore, computational analysis has revealed that over 27% of all electronic materials found in nature are topologically non-trivial [2]. Similar classification efforts have recently been made for photonic crystals [16].

The discovery of topological phases of matter and phase transitions has given physicists an entirely new understanding of material structure and behavior. It has led to a paradigm shift in condensed matter research, and has even begun to make its way into engineering as a means of imparting robustness in devices [1, 17, 18]. However, nothing better signifies the impact of an achievement than a Nobel Prize, which David Thouless, Michael Kosterlitz, and Duncan Haldane were jointly awarded in 2016 their contributions to the field of Physics [13].

1.1.2 The Su-Schrieffer-Heeger model

The Su-Schrieffer-Heeger (SSH) model is widely regarded as the simplest model that exhibits non-trivial topological behavior. The model concerns polyacetylene, a simple polymer chain with a unit cell that can be represented as two lattice sites connected by alternating hopping/coupling strengths [19]. Fig. 1.2a depicts both the chemical structure of this polymer and a tight-binding model representation. Here, the intra-cell (i.e., within the unit cell) coupling strength is denoted as “v” and inter-cell (i.e., between unit cells) coupling strength is denoted as “w.” The topological phase of the 1D insulator is determined by the relationship between these two parameters.

If $v > w$, the insulator is in its topologically trivial phase. In this phase, the SSH chain will behave like a conventional insulator– its energy spectrum will exhibit a band gap. As w approaches v, the band gap will decrease until it finally closes when $v = w$. If w continues to increase and becomes larger than v, the SSH chain enters its topologically non-trivial phase. Thus, $v = w$ represents the topological phase transition point for this system. Fig. 1.2b pictorially summarizes these results.

When the SSH chain enters its topologically non-trivial phase, the *bulk* band gap reopens and edge states appear at both ends of the 1D chain [19]. In this model, chiral symmetry fixes the energy of the edge states at the mid-gap energy of the bulk band gap [19]. This causes the edge states to be spectrally isolated from the bulk modes.

To calculate the band structure of this model, the Hamiltonian in equation 1.1 is constructed using the tight-binding model [19, 20]. This model assumes that the wave function associated with each site is dominantly localized to that site and only weakly interacts with its neighbors. The strength

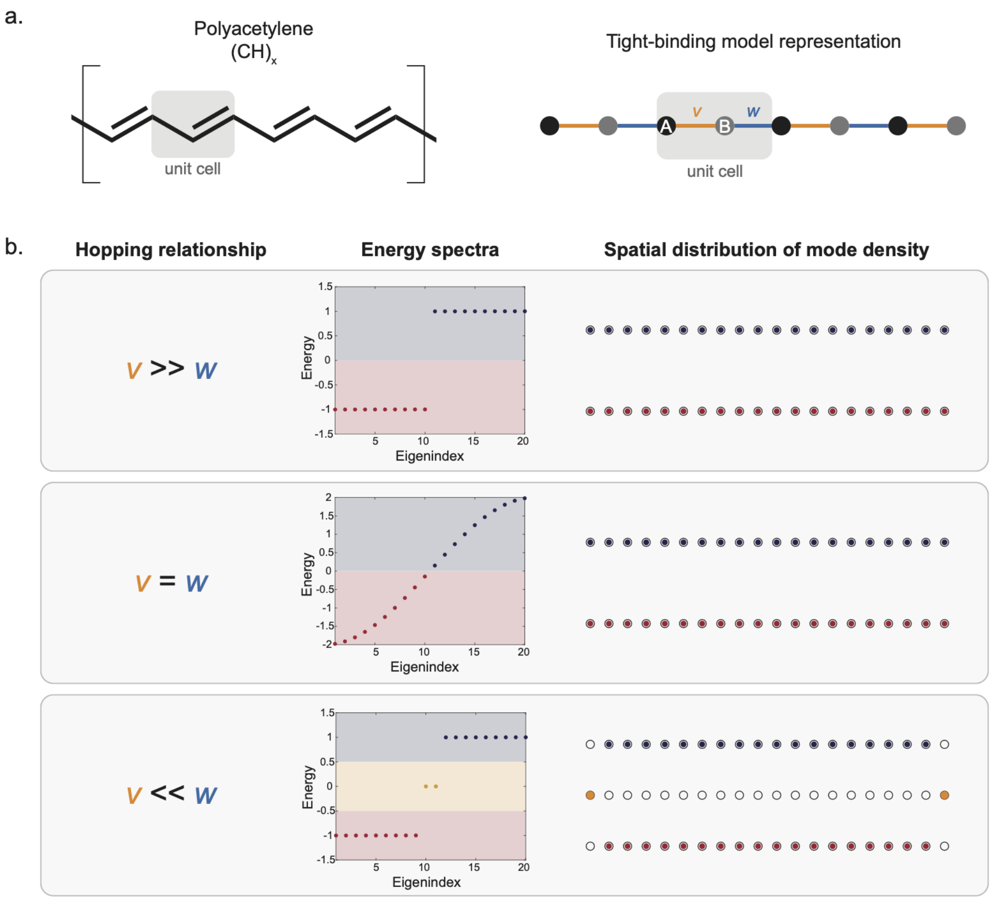

Figure 1.2: SSH model. **(a)** Chemical structure of polyacetylene and tight-binding model representation. Black (gray) circles denote sublattice sites A (B), and orange (blue) lines denote hopping strength w (v). **(b)** Representative examples of topologically trivial phase ($v >> w$), phase transition point ($v = w$), and topologically non-trivial phase ($v << w$) for a 10-unit-cell-long (N = 20 sites) SSH chain with open boundary conditions.

of these interactions is quantified by a hopping/coupling strength, which acts as a perturbation to the participating wave functions. For a system with N-sites, a $N \times N$ matrix can be defined that tabulates these results. The indices of each matrix element directly corresponds to the indexed sites. Thus, the diagonal element H_{ii} represents on-site energy at site i, and the off-diagonal element H_{ij} corresponds to the coupling between sites i and j. The Hamiltonian in equation 1.1 only considers nearest-neighbor coupling, which forms a tridiagonal matrix. In the absence of on-site energy, the main diagonal is composed of zeros.

$$\hat{H} = \begin{pmatrix} 0 & v & 0 & \cdots & 0 & 0 & 0 \\ v & 0 & w & \cdots & 0 & 0 & 0 \\ 0 & w & 0 & \cdots & 0 & 0 & 0 \\ \vdots & 0 & v & \ddots & v & 0 & \vdots \\ 0 & 0 & 0 & \cdots & 0 & w & 0 \\ 0 & 0 & 0 & \cdots & w & 0 & v \\ 0 & 0 & 0 & \cdots & 0 & v & 0 \end{pmatrix} \tag{1.1}$$

The Hamiltonian matrix represents an eigenvalue problem (equation 1.2) and can simply be diagonalized to obtain the energy eigenvalues (E_n) and eigenvectors (ψ_n).

$$\hat{H}\psi_n = E_n\psi_n \tag{1.2}$$

The energy spectra (Fig. 1.2b) is obtained by sorting the eigenvalues and plotting them as a function of the eigenindices. The spatial distribution of mode density for a given spectral band (Fig. 1.2b) is determined by summing $|\psi_n|^2$ over a range of energy, and then plotting the magnitude on the indexed sites.

The bulk Hamiltonian can also be expressed using a momentum-space basis, which relies on the periodicity of the unit-cell structure to produce a more compact notation [20, 19]. This compactness is a consequence of the Bloch theorem, which states that the wave function solution to a system subject to a period potential (e.g., a crystalline lattice) will take the form of a plane wave modulated by a periodic potential [20, 21]. This result is shown in equation 1.3, where $e^{i\mathbf{k}\cdot\mathbf{r}}$ is a plane wave, and $u(\mathbf{r})$ is a part of the wave function that has the same periodicity as the lattice.

$$\psi(\mathbf{r}) = e^{i\mathbf{k}\cdot\mathbf{r}}u(\mathbf{r}) \tag{1.3}$$

This result can be extended to momentum space by performing a Fourier transform to obtain equation 1.4, which indicates that the u term in the wave function is also periodic in the Brillouin zone [20].

$$|u(k+2\pi)\rangle = |u(k)\rangle \tag{1.4}$$

Combining these results and applying them to the SSH model yields the bulk Hamiltonian in equation 1.5 [20], where w is the intra-cell hopping, and v is the inter-cell hopping from Fig. 1.2.

$$\hat{H}(k) = \begin{pmatrix} 0 & v + we^{-ik} \\ v + we^{ik} & 0 \end{pmatrix} \tag{1.5}$$

It follows that this Hamiltonian obeys the relationship in equation 1.6, which allows the bulk band structure can be determined by a single Brillouin zone [20].

$$\hat{H}(k + 2\pi) = \hat{H}(k) \tag{1.6}$$

The momentum-space form of the Hamiltonian allows for the bulk dispersion relation to be calculated from equation 1.7 [20].

$$\hat{H}(k)^2 = E(k)^2 \begin{pmatrix} 1 & 0 \\ 0 & 1 \end{pmatrix} \tag{1.7}$$

Applying this relationship to equation 1.5 yields equation 1.8 [20].

$$E(k) = |v + e^{-ik}w| = \sqrt{v^2 + w^2 + 2vwcos(k)} \tag{1.8}$$

These results are shown in Fig. 1.3a for the following cases: the topologically trivial phase ($v > w$), the phase transition point ($v = w$), and the topologically non-trivial phase ($v < w$). The topological invariant of this model, known as the bulk winding number, is also plotted in Fig. 1.3b. The winding number is a topological integer quantity determined by how many times the loop traced by the bulk Hamiltonian, $\hat{H}(k)$, winds around the origin, $h_x(k) = 0$, $h_y(k) = 0$.

In this model, if $v > w$, the winding number is 0 and the system is in its topologically trivial phase. When $v = w$, the loop traced by the bulk Hamiltonian passes through the origin, and the winding number is undefined [20]. When $v < w$, the loop traced by the bulk Hamiltonian encompasses the origin. This means that the winding number is 1 and the system is in its topologically non-trivial phase. In this phase the insulator will host topologically protected edge-localized states [20]. These states are said to be protected because they are a manifestation of the system's topology and are robust to any perturbation that does not close the bulk band gap (and thus change the system's winding number).

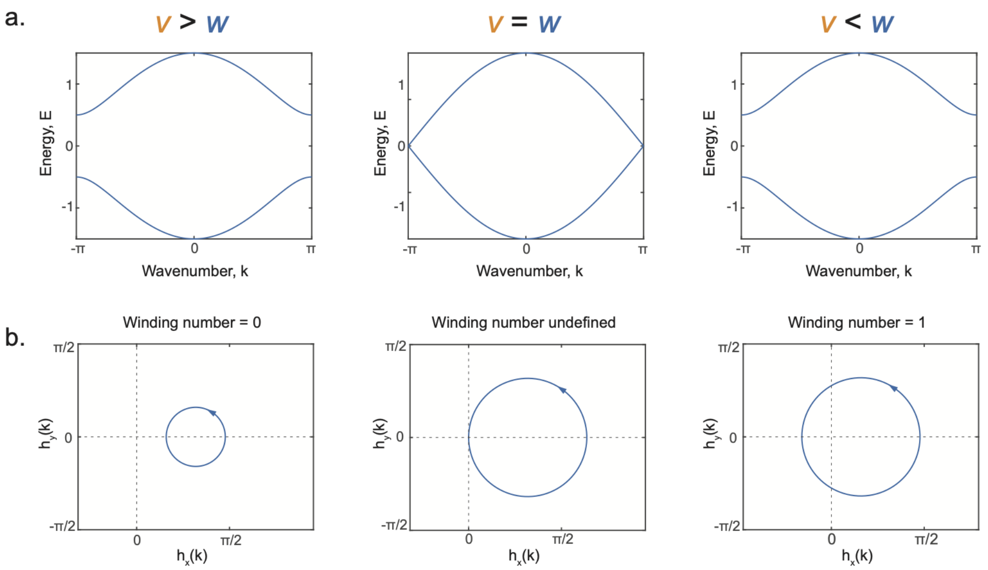

Figure 1.3: Dispersion and winding of the bulk Hamiltonian of the SSH model. **(a)** Dispersion relations of topologically trivial phase ($v \gg w$), phase transition point ($v = w$), and topologically non-trivial phase ($v \ll w$) for the SSH model. **(b)** Winding of bulk Hamiltonian for the same cases in (a).

1.1.3 Multipole topological insulators

This thesis focuses on a particular class of topological crystalline insulators (TCIs) characterized by quantized electric multipole moments [22, 23]. These TCIs are used as model-specific examples to investigate how crystallographic defects interact with topology. The topology of this set of insulators is protected by quantized multipole moments, giving them their namesake [24, 25]. These multipole moments are similar to those from classical electromagnetics, but differ in that they are quantized by symmetries of a crystalline lattice [22, 23, 24].

The 2D and 3D quantized electric multipole insulators, known as quadrupole and octupole insulators, are the primary focus of the experiments described in this thesis. The classical charge distributions associated with these insulators, along with the minimal models that realize their quantized version, are shown in Fig. 1.4. It can also be noted that the SSH model (Section 1.1.2) is the minimal model for a 1D dipole insulator [19, 24].

In the tight-binding diagrams shown in Fig 1.4b, the 2D quadrupole and 3D octupole unit cells have negative coupling between sites. This is negative coupling pattern realizes a π-flux threading through each plaquette and is required to open a bulk band gap in the models [9, 24, 25]. This is achieved by setting an odd number of coupling links around any four-site loop to be negative [24]. In the quadrupole case, one coupling is set to be negative, which is sufficient for a 2D model. In the octupole case, four couplings must be negative to ensure a π-flux threading along each direction of the lattice.

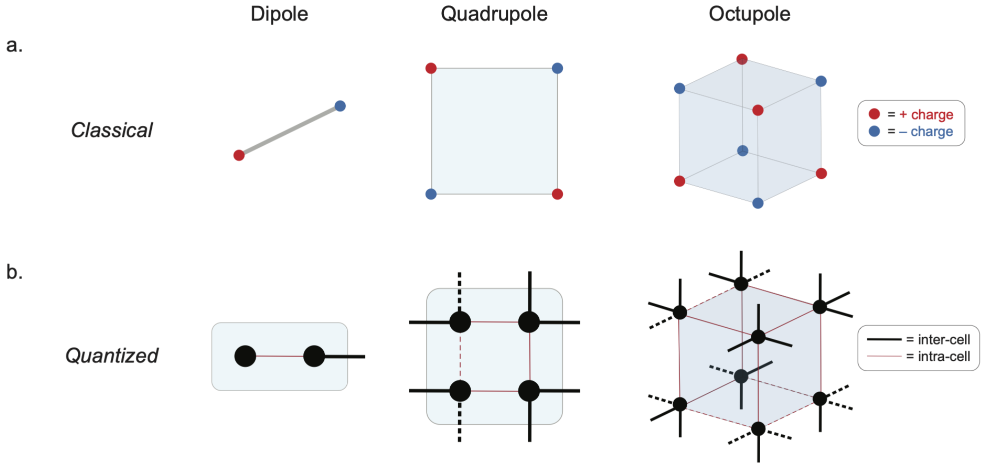

Figure 1.4: Multipole insulators, inspired by [24]. (a) Depiction of multipole moments from classical electromagnetics **(b)** Tight-binding diagrams of the minimal models that realize quantized electric multipole moments. Here, the black circles represent lattice sites, and the inter-cell (intra-cell) coupling is denoted by the black (red) lines. The dashed lines indicate negative coupling between sites.

Electric multipole insulators are classified as *higher-order* topological insulators because their topologically protected features occur at higher-order material boundaries. The "order" of each feature follows the hierarchy shown in Fig. 1.5. From this figure, it can be noted that the order of a topological feature cannot exceed the dimension of the material. For the quantized multipole insulators considered in this thesis, the order matches the dimension of the material. Thus, each multipole insulator will exhibit 0D topological modes localized to the highest-order boundaries (i.e., the corners). Similar to the SSH model discussed in the previous section, these boundary modes appear at the mid-gap energy of the bulk band gap when chiral symmetry is preserved [24]. However, in many experimental systems the presence of loading and chiral-symmetry breaking causes the energy of the corner modes to deviate from this [9]. This is also the case for the experiments discussed in this thesis.

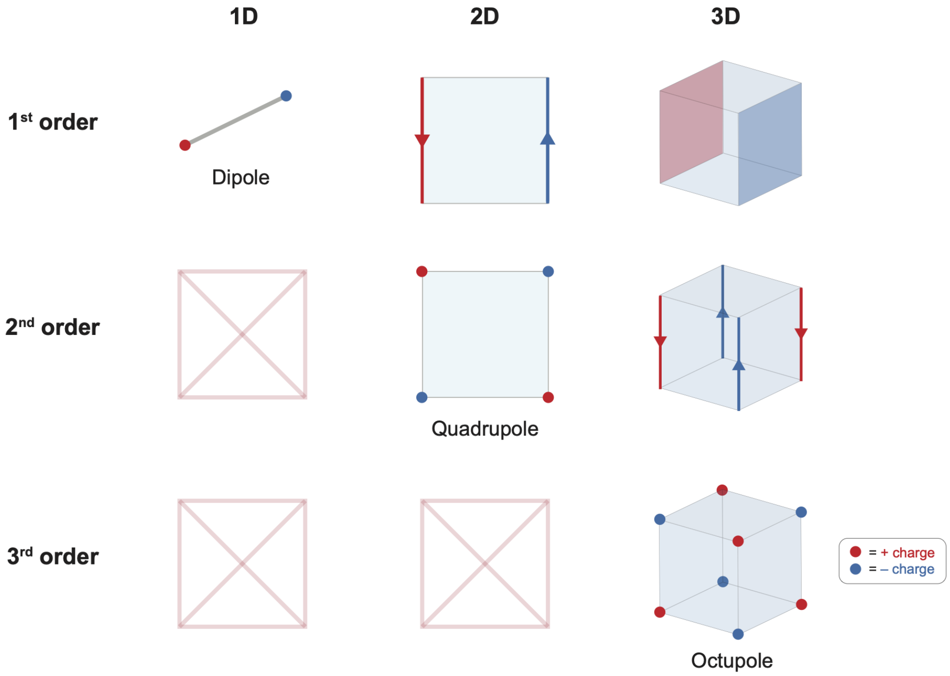

Figure 1.5: Hierarchy of topological insulators, inspired by [26]. A grid illustrating allowed topological features for various dimensions of topological insulators is shown. The order of each topological feature cannot exceed the dimension of the material (e.g., there are no 1D topological insulators with 2nd-order topology, so this element is crossed out with a red box). The corner-localized circles correspond to 0D topological modes, the edge-localized lines with arrows correspond to 1D topological modes, and the surface-localized planes correspond to 2D topological modes.

1.2 Motivation & scope

As discussed in the sections above, topological insulators represent a unique class of materials with unusual transport properties. It is perhaps then no surprise that these materials have caught the attention of engineers looking to make their devices more robust. Over the past several years, a symbiotic relationship has developed between physicists and engineers working together to advance topological materials research. The use of metamaterial systems has drastically reduced the turnaround time between theory and experiment. Additionally, their precise construction has allowed for specific interactions—like those of isolated defects—to be studied [27, 28, 29]. Conversely, engineers have benefited from exposure topological phenomena like back-scatter immune waveguiding [15] and robust protected states [12], which can inform the design of novel devices.

The best example to date of a device that has leveraged non-trivial topology is the topological laser [17, 18, 30]. While still in its infancy in terms of technology development, the topological laser has the potential to produce efficient single-mode emission with narrow linewidths [18]. Back-scatter free, unidirectional waveguiding has also been demonstrated in a metamaterial system [15]; however, the specific implementation used is not realistic for applications.

While the protected boundary states of topological insulators have native robustness, they are still vulnerable to certain perturbations. For example, if you were to remove the edge sites of an SSH chain (Section 1.1.2), its topological phase would change. Of course this represents a significant modification to a simple material, but it illustrates that these topological states are not indestructible. It is also important to consider that these protected states require some finite bulk structure to exist. The minimum necessary size of this bulk structure is model-specific, but in general it must be large enough to prevent boundary states on opposite sides of the material from coupling to each other. This requirement is a disadvantage with respect to footprint size for potential devices. With these issues in mind, it would then be desirable to embed topologically protected states within the bulk structure of a material, as doing so would better shield the mode from external perturbations and make more efficient use of the bulk material.

This thesis experimentally investigates the use of partial dislocation defects to trap bound states in topological insulators. To achieve this, modular circuit-based metamaterials were constructed and characterized. These metamaterials were used to realize 2D quadrupole and 3D octupole insulators, as well as their respective partial dislocation defects. After characterizing each metamaterial, protected corner modes and bound states were observed at the partial dislocation defect cores. These observations verify that partial dislocation defects interact with the topology of multipole TCIs and can trap bound states. Although specific models of multipole insulators are considered here, the results of this study extend to other models as well.

The structure of this thesis is as follows– Chapter 2 introduces common crystallographic defects and summarizes previous work regarding how these defects interact with topology. This chapter also introduces partial dislocation defects and describes how they can trap bound states in topological insulators. Next, Chapter 3 briefly reviews topological metamaterials published in the literature and describes the construction of the circuit-based metamaterials considered in this thesis. This chapter also details the measurement procedure used to characterise the metamaterials. Chapter 4 presents the experimental results of this study. This chapter provides measurements that verify the multipole behavior of the constructed metamaterials, as well as their ability to trap bound states at partial dislocation defects. Finally, Chapter 5 summarizes the work described in this thesis and proposes future work.

CHAPTER 2

CRYSTALLOGRAPHIC DEFECTS

In this chapter, crystallographic defects such as disclinations and dislocations will be described. These defects are ubiquitous in crystalline materials and can interact with non-trivial topology to produce trapped states [27, 31, 32, 33] and fractional charges [28, 29, 34, 35, 36, 37]. In addition, partial dislocation defects will be introduced and their ability to trap fractional charge and bound states in multipole TCIs will be explored.

2.1 Interaction of defects with topology

This section introduces common crystallographic defects and discusses their interaction with topology using a fractional charge perspective.

2.1.1 Fractional charge

Topological insulators with invariants quantized by crystalline symmetries (e.g., multipole TCIs) can exhibit a filling anomaly which results in *fractional* charge (per unit cell) at its boundaries [38]. This anomaly is the result of a mismatch between the number of electrons that occupy each energy band and the number of electrons required for charge neutrality [38]. Topological insulators that have C_n rotational symmetry will exhibit fractional charge quantized in multiples of $\frac{e}{n}$, where e is elementary charge [38]. This fractional charge can be experimentally accessed by measuring the spectral mode density, an analogous metric to fractional charge in classical systems (e.g., metamaterials) [28, 29, 39].

Charge fractionalization in TCIs can be intuitively understood by considering the Wannier representation of each unit cell. Since TCIs by definition have periodic structure, the wave functions of each site can be represented by Bloch functions (see Section 1.1.2) [21]. These Bloch functions can then be expressed as localized Wannier orbitals in a real-space basis [38, 40]. In materials with crystalline symmetries, these Wannier orbitals can only be localized at a finite number of points in each unit cell. For example, the SSH model (Section 1.1.2) is described using Wannier orbitals in Fig. 2.1. Since each unit cell of this model is reflection symmetric, there are two possible positions that the bulk Wannier orbitals can be localized to in each unit cell: at the center (Fig. 2.1a, green) or at the edges (Fig. 2.1a, blue) [38]. These possible positions are high-symmetry points of the real-space lattice and are known as the maximal Wyckoff positions [38].

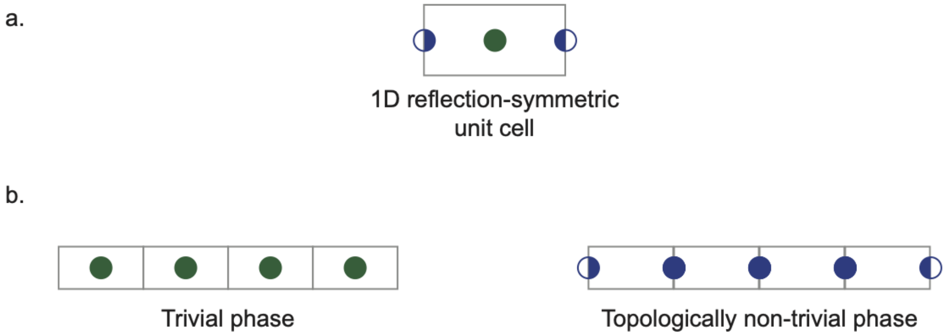

Figure 2.1: Wannier center configurations for SSH model. (a) Each filled circle represents the elementary charge e. Partially filled circles represent fractional charge. Each circle is centered a high-symmetry point corresponding to a localized Wannier orbital that maintains reflection symmetry. **(b)** Possible Wannier orbital configurations when half of the energy bands are filled. When the Wannier orbitals are centered in the middle of each unit cell, the SSH chain is in a topologically trivial phase. When the Wannier orbitals are localized to the edges of each unit cell, the SSH chain is in a topologically non-trivial phase, resulting in quantized fractional charge $\frac{e}{2}$ at its edge unit cells.

To determine if a TCI exhibits a (charge) filling anomaly, the Wannier representation of the insulator when half of the energy bands are filled is considered. This condition is often referred to as "half-filling," and corresponds to the Fermi level (or chemical potential) being fixed at the energy in which half of the available states in a system are filled. The SSH model only has two bulk energy bands, so its half filling is evaluated at its mid-gap energy. The Wannier representation of the SSH model at half filling is shown in Fig. 2.1 and uses (partially) filled circles to represent (fractional) charge per unit cell. Fig. 2.1b shows the two possible configurations of the Wannier orbitals for an SSH chain with four unit cells. In the topologically trivial case, the Wannier orbitals are centered at the middle of each unit cell, and there is no charge imbalance. In the non-trivial case, the Wannier orbitals are centered at the edges of each unit cell, causing charge imbalance to occur. As a result, fractional charge of $\frac{e}{2}$ per unit cell can be observed at the edges of the TCI.

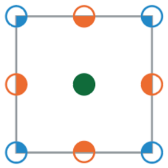

Configuration Properties			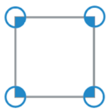
Charge/unit cell $Q_{u.c.}$ [e]	1	2	1
Polarization (P_x,P_y) [e]	(0,0)	(1/2,1/2)	(1/2,1/2)
Topological property	Trivial	1st order TI	Higher-order TI

Figure 2.2: Wannier center configurations for a C_4 lattice. Each filled circle represents the elementary charge e. Partially filled circles represent fractional charge. Each circle is centered a high-symmetry point corresponding to a localized Wannier orbital that maintains C_4 rotational symmetry.

The possible Wannier center configurations for a C_4 symmetric TCI are shown in Fig. 2.2. The topology of these C_4 TCIs depends on where the Wannier orbitals are localized in each unit cell. If each Wannier orbital is centered in the middle of each unit cell, the TCI is topologically trivial. However, if the Wannier orbitals are localized to the edges (corners) of each unit cell, then the TCI exhibits first-order (higher-order) topological features [38]. This is a consequence of the charge filling anomaly which quantizes fractional charge localized at the boundaries of TCIs [38]. The C_4 symmetric TCI with Wannier centers localized to the corners of each unit cell is a higher-order TCI and is used as an example in Sections 1.1.2 and 1.1.3 to illustrate how disclination (rotational) and dislocation defects trap fractional charge at their defect cores.

2.1.2 Disclinations

Disclinations are rotational lattice defects that are formed by a deficit or excess of a rotational sector. Fig. 2.3 shows two examples of C_4-symmetric TCIs with disclination defects; the resulting lattices are C_3- and C_5-symmetric. Since the original lattice has C_4 symmetry, each rotationally symmetric sector forms a $\frac{\pi}{2}$ angle. When adding or subtracting a sector to form a disclination defect, the angle of that sector is known as the Frank angle (Ω) and carries a sign that indicates how it modifies the original lattice [41]. For example, $\Omega = -\frac{\pi}{2}$ for the C_3 lattice and $\Omega = \frac{\pi}{2}$ for the C_5 lattice in Fig 2.3.

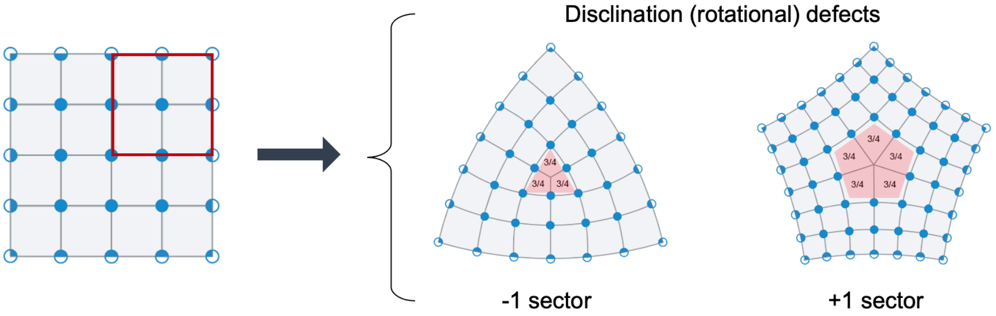

Figure 2.3: Depiction of disclination defects in C_4 lattice. The Wannier representation of each lattice is shown. For the disclinated lattices, the fractional charge per unit cell trapped at the defect core is labeled. The defect core is highlighted in red.

It has been shown that disclination defects can trap fractional charge at their defect cores in TCIs [28, 29, 38, 41, 42, 43, 44]. This effect can be understood by considering the Wannier representation of the disclinated TCI lattices and counting the charge contribution of each Wannier center. The defect cores in Fig. 2.3 (highlighted in red) label the fractional charge contribution per unit cell in units of e when half of the energy bands are filled. This fractional charge can either be measured via the spectral mode density, or it can be combined to form an isolated bound state [28, 29, 39]. It follows that disclination defects can serve as a bulk probe of a topology in TCIs [28, 29, 41].

However, the use of disclination defects as as bulk probe has some notable shortcomings. The analysis above focuses on isolated disclination defects, which are not energetically favorable in solid state materials. This significantly limits their use as a bulk probe in 2D materials research. In engineered materials (like metamaterials), single disclination defects also require massive rearrangement of the global lattice structure. This effect is more obvious for larger lattices (Fig. 2.4). Furthermore, in the context of the multipole models considered in this thesis, disclination defects may bind fractional charge in 2D quadrupole insulators but are not guaranteed to do so in 3D octupole insulators.

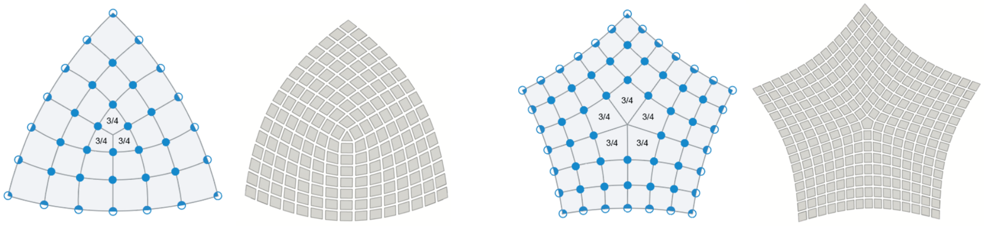

Figure 2.4: Illustration of how single disclination defects warp a crystalline lattice. Disclinated C_4 lattices are shown with Frank angles $\Omega = \pm\frac{\pi}{2}$.

2.1.3 Dislocations

Dislocation defects are formed by an excess or deficit of complete unit cells. These defects are characterized by a quantity known as the Burgers vector, which quantifies the difference in the number of translations required to trace a loop around an ordinary point of the lattice compared to tracing a loop around a dislocation core. When a dislocation core replaces the ordinary point, then the original loop that was traced around the ordinary point fails to perfectly close, and the deficit or excess in the displacement is the Burgers vector [37, 45]. Disclination defects are another type of crystallographic defect that have been shown to trap fractional charges and bound states in TCIs [27, 31, 32, 36, 46, 47, 48, 49].

Fig. 2.5 shows an example of a dislocation defect in a C_4 TCI formed by a deficit of complete unit cells. Similar to the disclination defects discussed in the previous section, the Wannier representation of the TCIs are shown. The same counting procedure is then applied to find the fractional charge contribution per unit cell at the defect core. From this analysis it is clear that dislocation defects can also trap fractional charge at their defect cores.

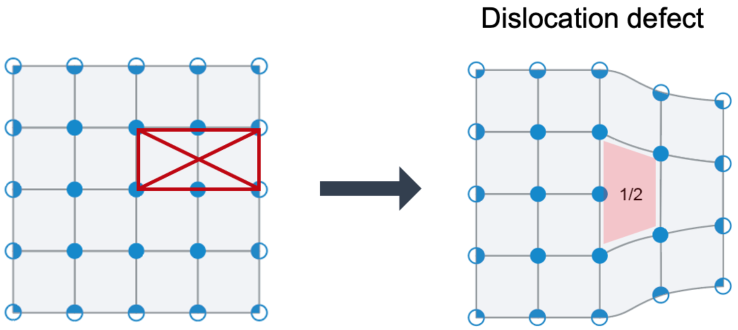

Figure 2.5: Depiction of dislocation composed of complete unit cells in a C_4 lattice. The Wannier representation of each lattice is shown. The defect core is highlighted in red and the fractional charge per unit cell is labeled.

However, dislocation defects do not trap fractional charge or bound states in the quadrupole insulators considered in this thesis. Fig. 2.6 illustrates the Wannier representation of a C_4 TCI with and without vanishing polarization (P_x, P_y) per unit cell. The lattice with vanishing polarization is the Wannier representation of a quadrupole TCI, and it has two Wannier orbitals at each high-symmetry point in its lattice. It follows that, each (green) circle in its Wannier representation corresponds to two charges. Counting the fractional charge contribution per unit cell in each lattice leads to the conclusion that dislocation defects in C_4 TCIs with vanishing polarization do not trap fractional charge and thus cannot be used as a bulk probe.

2.2 Partial dislocation defects

Partial dislocation defects are similar to the dislocation defects discussed in Section 2.1.3, but differ in that they are composed of incomplete unit cells. This implies that partial dislocation defects are characterized by Burgers vectors that are a fraction of a lattice translation vector [45]. To clearly distinguish between partial dislocations and the dislocations discussed in Section 2.1.3, the latter will be referred to as *full* dislocations for the remainder of this thesis.

Partial dislocations can intuitively be thought of as a fractional decomposition of a full dislocation (Fig. 2.7). These defects can occur naturally in solid-state systems and are formed by the insertion of lines/planes of incom-

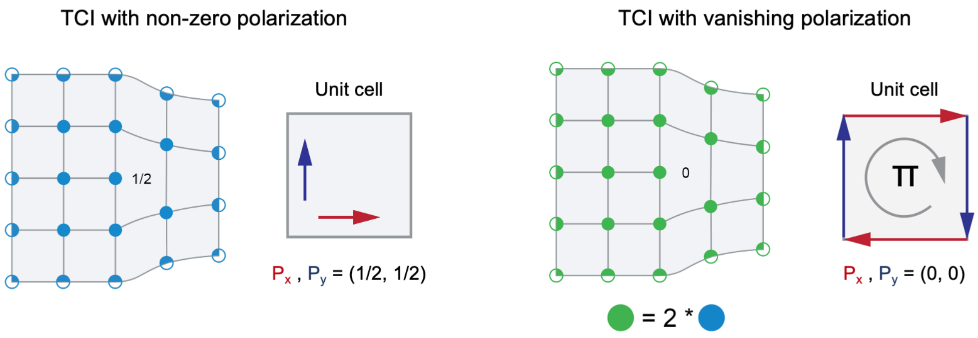

Figure 2.6: Showing that dislocations do not trap fractional charge in TCIs with vanishing polarization. The Wannier representation of each lattice is shown. Each blue circle represents a single Wannier orbital with total charge e. Each green circle represents two Wannier orbitals with total charge $2e$. When the fractional charge contribution per unit cell is tallied, the TCI with vanishing polarization does not have any fractional charge (modulo 1) trapped by its defect core.

plete unit cells in a 2D/3D lattice. Partial dislocations are also intimately related to stacking faults. If a stacking fault spans only a portion of the entire crystal plane, its boundary point/line is a partial dislocation in 2D/3D. It follows that these definitions restrict the scope of this thesis to topological realizations that have spatially distributed sublattice degrees of freedom so that stacking faults and partial dislocations can exist.

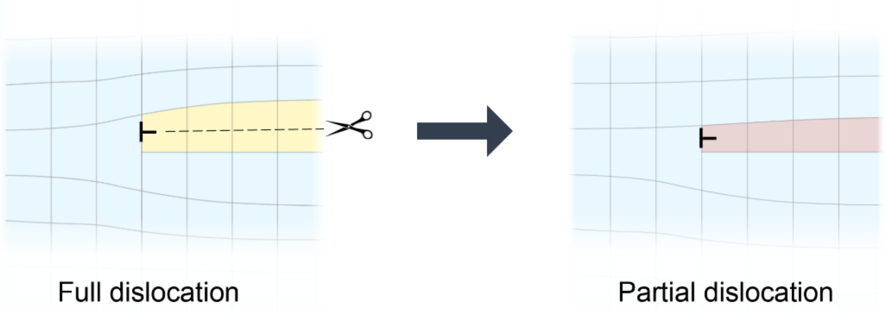

Figure 2.7: Intuitive depiction of a partial dislocation defect. These defects can be viewed as a fractional decomposition of a full dislocation

It has recently been proposed that partial dislocation defects can trap gapless states in some topological materials [45, 50]. The following paragraphs provide an intuitive argument that explains why these defects can trap bound states in multipole TCIs. As a specific example, consider the 2D quadrupole insulator model from Section 1.1.3 (Fig. 2.8a). This model has four degrees of freedom per unit cell and a π-flux threading through each plaquette. Different choices of the intra- and inter-cell couplings change the topology of the material. It follows that there are four natural gapped configurations for this TCI, of which only the one having weak intra-cell coupling in both directions has a non-zero, quantized quadrupole moment per unit area of $q_{xy} = \frac{1}{2}$, in units of elementary charge e [25].

Let us now consider a non-trivial quadrupole TCI with unit cells having $q_{xy} = \frac{1}{2}$ (Phase I in Fig. 2.8a). To construct a partial dislocation defect, a row of partial unit cells is inserted into the lattice (Fig. 2.8b). This dislocation defect is characterized by a fractional Burgers vector $\mathbf{B} = (\frac{1}{2})\hat{y}$ in units of lattice constant (left panel of Fig. 2.8b). To clearly illustrate the effect of the partial dislocation, the unit cells in one quadrant are redefined to incorporate the dislocation defect, and to once again form complete quadrupolar unit cells. It is important to note that this is simply a change of perspective and the micro-structure of the lattice is not modified in any way. For the example in Fig. 2.8b, the partial dislocation is grouped with the lower right quadrant of the lattice. Compared to the original unit cells (Phase I in Fig. 2.8a), the redefined unit cells in the lower right quadrant are in Phase II and no longer host a non-trivial quadrupole moment. This illustrates that the partial dislocation has introduced a spatial phase boundary between a trivial and non-trivial quadrupole TCI. As a result, fractional charge and a 0D topological bound state are expected to be localized at the higher-order boundaries (i.e., the corner of the phase boundary), which sits at the dislocation core.

This argument can be similarly extended to 3D octupole TCIs having partial dislocation planes. For this example consider the octupole TCI introduced in Section 1.1.2, which is composed of unit cells with eight degrees of freedom. In the configuration where all of the x, y, z inter-cell couplings are stronger than the respective intra-cell couplings, the TCI hosts a non-trivial octupole moment $o_{xyz} = \frac{1}{2}$, in units of elementary charge e [25]. A partial dislocation can then be added by inserting a plane composed of half of the octupole model's unit cells into the original lattice. The edge of the inserted plane is a partial dislocation line, and the Burgers vector associated with that line is $\mathbf{B} = \frac{1}{2}\hat{z}$ in units of the lattice constant. Similar to the quadrupole

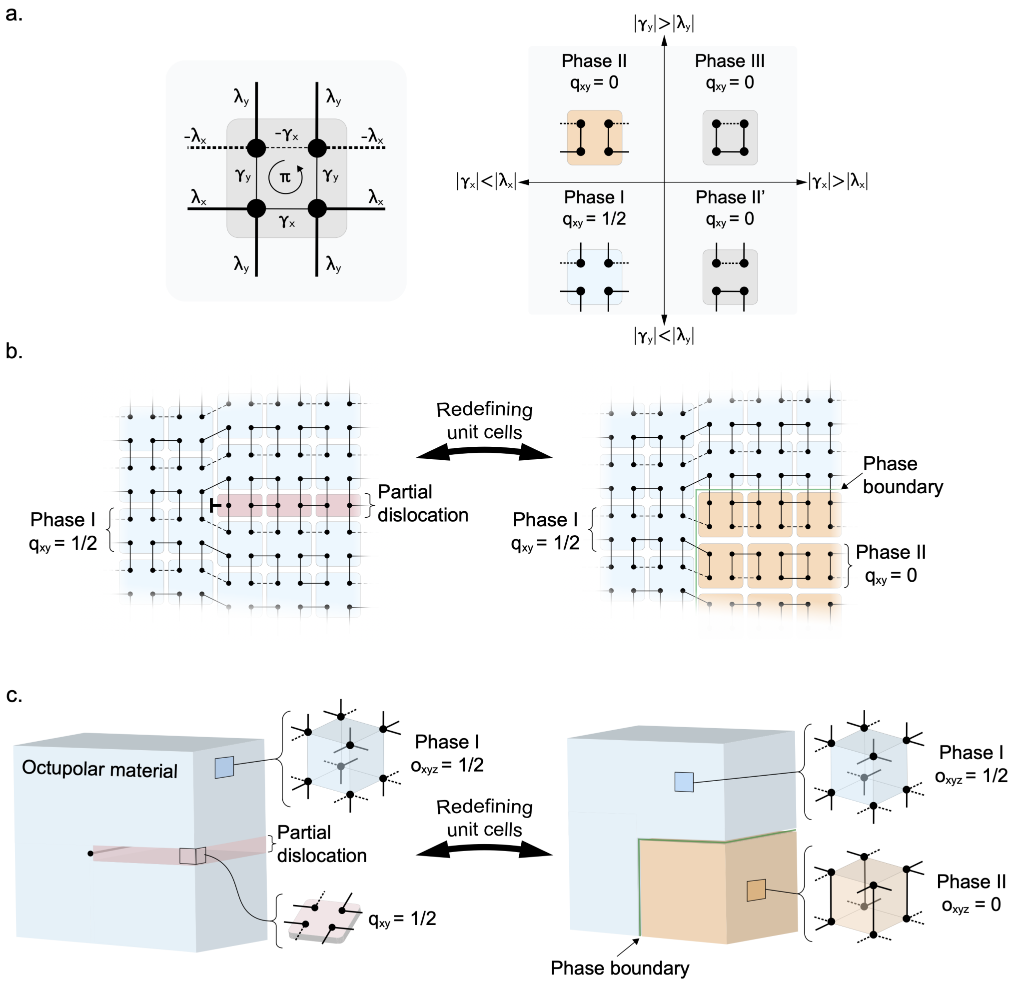

Figure 2.8: Origination of topological phase boundaries due to partial dislocations in 2D and 3D multipole TCIs. (a) Possible connections in the minimal model of single quadrupole TCI unit cell and corresponding topological phase diagram. Intra-cell couplings are labeled as $\gamma_{x,y}$ and inter-cell couplings are labeled as $\lambda_{x,y}$. The dashed lines denote negative coupling. The dimerized limit is illustrated in the phase diagram, so only the dominant connections are shown. **(b)** Equivalence between quadrupole TCI (blue unit cells) in the topological phase with partial dislocation (red unit cells) and phase boundary between trivial (orange unit cells) and non-trivial (blue unit cells) quadrupole phases. The dislocation core is denoted as $\vdash$. The unit cells are depicted in their dimerized limit. **(c)** Same as (b), but for an octupole TCI. Here, the partial dislocation is a plane defect and thus terminates along a line within the bulk. The unit cells shown in the inset are depicted in their dimerized limit.

TCI case, the unit cells are redefined to group the partial dislocation with the lower right sector as shown in Fig. 2.8c. After performing this operation, the redefined unit cells no longer host a non-trivial octupole moment, and the partial dislocation forms a phase boundary with the original lattice configuration. Thus, 0D topological bound states are expected to be localized at locations where the dislocation line terminates on a surface, or if it is closed, where the dislocation line makes a 90 degree turn to form a corner.

Although this discussion considered specific models in simple limits, these arguments can be generalized to any insulator where stacking faults act as spatial domain walls between trivial and obstructed atomic insulators. Indeed, such insulators will exhibit localized fractional charge at partial dislocation defect cores. A large class of such insulators, i.e., those composed of lower-dimensional topological subsystems (e.g., embedded topological insulators) are expected to be responsive to partial dislocation defects [50]. Remarkably, such insulators may trap bound states, even if the overall system is nominally topologically trivial. An example of this situation is shown in Fig. 2.9.

Additionally, to serve as a bulk probe of higher-order topology, partial dislocations can be used to characterize the fractional corner anomaly [38, 39]. For example, the 2D quadrupole TCI studied here traps fractional charge (or bound states) at the defect core of both $\hat{x}$- and $\hat{y}$-oriented partial dislocations, and thus manifests a fractional corner anomaly (Fig. 2.10). In general it is expected that defects with Burgers vectors along the different crystal directions of the material which naturally meet at a corner will trap fractional charge consistent with the fractional corner anomaly of the obstructed atomic limit phase [38, 39].

a.

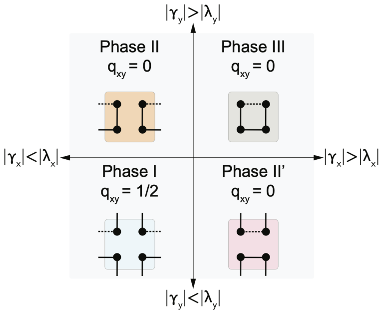

b. **Partial dislocation inserted into nominally topologically trivial phase**

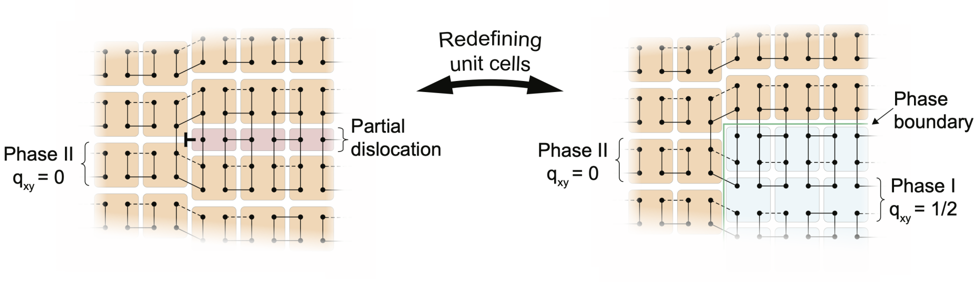

Figure 2.9: Illustration of partial dislocation defect in a nominally topologically trivial lattice. (a) Phase diagram of quadrupole TCI **(b)** A partial dislocation oriented along $\hat{x}$-direction of a nominally trivial quadrupolar TCI (converse of the case studied in main text) also forms a phase boundary and thus traps a bound state at the higher-order point (i.e., corner) of that boundary. It should be noted that a partial dislocation oriented along $\hat{y}$-direction will yield a phase boundary between phase II and phase III unit cells. In this case, the quantized quadrupole moment per unit cell is zero for both phases, hence no bound states will be trapped at the partial dislocation defect core.

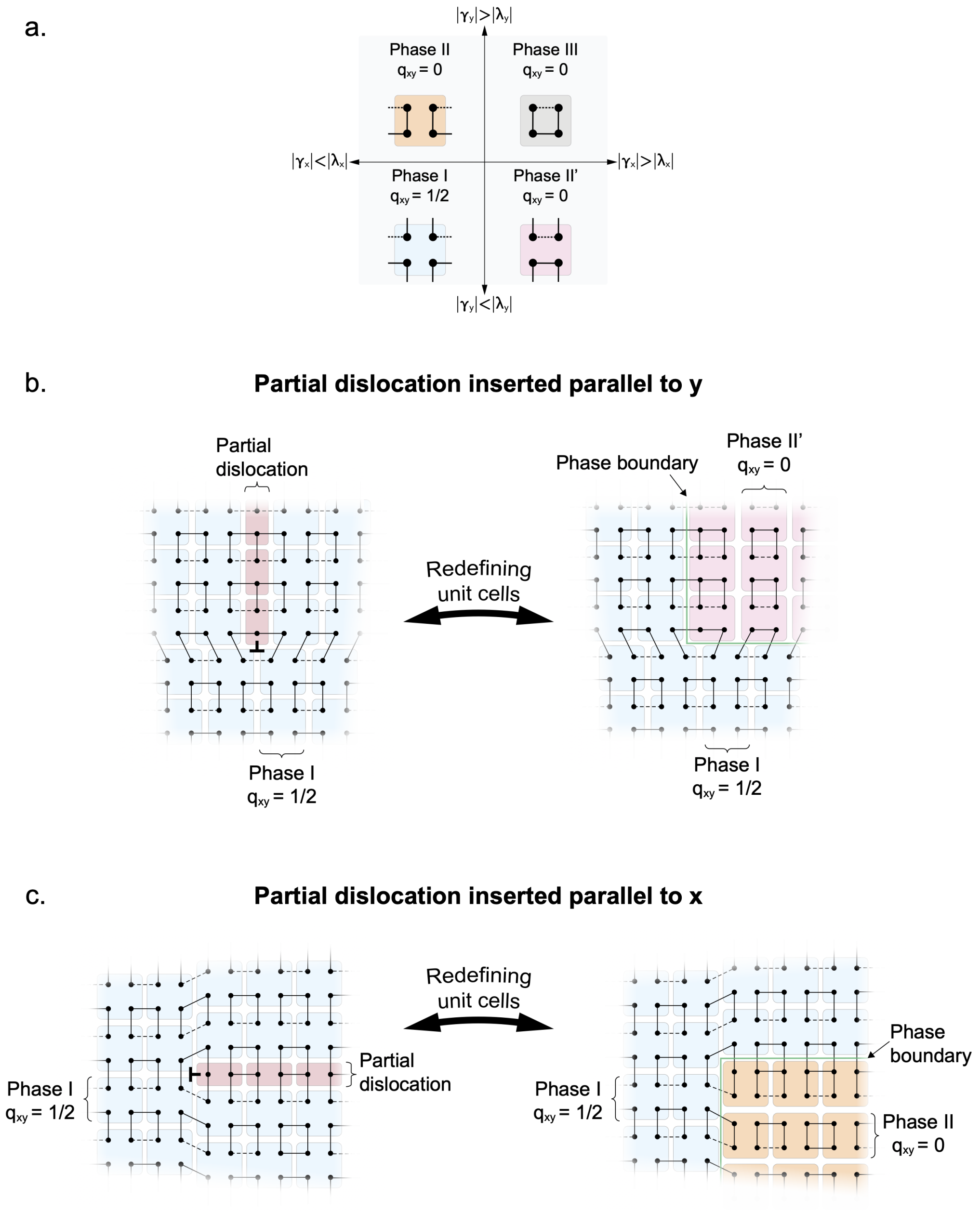

Figure 2.10: Visualization of criteria for partial dislocation to probe the higher-order topology of a quadrupolar TCI. (a) Phase diagram of quadrupole TCI **(b)** Partial dislocation oriented along $\hat{y}$-direction, which forms a phase boundary between topologically trivial (phase II') and non-trivial (phase I) regions. Since the quantized quadrupole moment per unit cell is different in these two regions, a bound state will be trapped at the higher-order point of their phase boundary. **(c)** Partial dislocation oriented along $\hat{x}$-direction of quadrupolar TCI (case studied in main text). For the same reasons as (b), this defect also traps a bound state. Since the quadrupole TCI in phase I traps bound states at partial dislocations oriented along both the $\hat{x}$- and $\hat{y}$- directions, it can be concluded that the insulator is a HOTI.

CHAPTER 3

TOPOLOGICAL METAMATERIALS

This chapter discusses how metamaterials can be used to construct topological materials. It begins with a brief survey of published literature concerning metamaterial implementations of topological materials. Next, the circuit-based metamaterial used in this thesis to investigate partial dislocation defects in multipole topological insulators is introduced.

Section 3.1 focuses on the operating principle of coupled-resonator metamaterials and explains how they can implement the Hamiltonian of a topological material. Section 3.2 focuses on the specific implementation of the circuit-based metamaterials considered in this thesis. This section also describes the measurement procedure used to characterize these systems.

3.1 Theory & construction

This section describes how topological materials can be implemented using metamaterials. Specifically, the relationship between coupled-mode theory and the tight-binding model is discussed in Section 3.1.1, and a circuit-implementation of the SSH model (Section 1.1.2) is used as an illustrative example. Alternative approaches from literature are summarized in Section 3.1.2.

3.1.1 A circuit implementation of the SSH model

Coupled mode theory is analogous to the tight-binding model [1, 12], making coupled-resonator systems a well-suited platform to construct topological insulators. In general, a coupled-resonator system can be constructed for a given tight-binding Hamiltonian using the following equivalencies: the resonance frequency of each resonator is proportional to the on-site energy at each site, the coupling between resonant modes is directly analogous to the coupling rate between sites, and any on-site potential or loading of a resonator can be accounted for as a perturbation to the on-site energy of a site.

One caveat is that the tight-binding Hamiltonian should be expressed in a real-space basis. However, this is not a serious issue, since a Hamiltonian in a different basis (e.g., k-space) can be transformed into the proper form using a change of basis. To illustrate the process of constructing a coupled-resonator metamaterial from a real-space Hamiltonian, the SSH model (Section 1.1.2) will be used as a concrete example. For simplicity, a lumped-element circuit model will be proposed.

To implement an SSH chain with N-sites (N/2 unit cells), N resonators are needed. These resonators can be constructed from basic inductor-capacitor (LC) circuits (Fig. 3.1). Each resonator is resonant at a frequency f_0, in which the impedance of the capacitor ($Z_C = \frac{1}{i\omega C}$) is equal to the impedance of the inductor ($Z_L = i\omega L$), where C is capacitance, L is inductance, and ω is angular frequency ($\omega = 2\pi f$). Each resonator can then be coupled to its neighbors using capacitors. The connectivity of these coupling links can be read directly off of the real-space Hamiltonian; for this example, the connectivity is given by equation 1.1. The capacitance of each component is directly related to the coupling strength (i.e., larger capacitance values result in stronger coupling/hopping). For the SSH model, two different strengths of capacitors are needed to realize the two different hopping strengths (v, w). The simplest coupled-resonator circuit that will realize the SSH model is shown in Fig. 3.1.

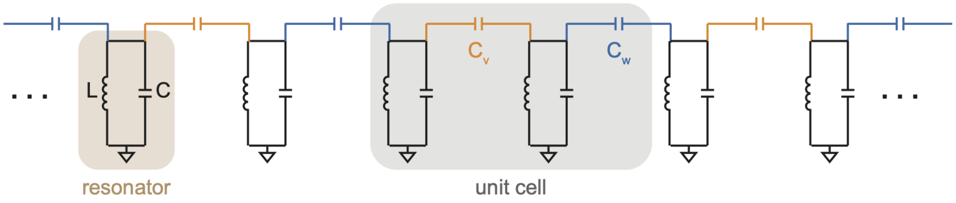

Figure 3.1: Circuit implementation of SSH chain. Coupled-resonator system implementing the SSH model described in Section 1.1.2. Each site is realized by an LC-resonator (highlighted in beige), and the coupling between sites is realized by capacitors. Two different capacitance values are needed to realize the two hopping strengths (v, w) in the model.

3.1.2 Approaches from literature

This section provides a brief summary of various approaches used to construct topological metamaterials published in literature. It is important to note that the implementation of any topological insulator must satisfy the model-dependent physics of that insulator. For example, to implementing topological insulators with non-zero Chern numbers (see Section 1.1.1) requires time-reversal symmetry to be broken [1, 12, 15]. This has been experimentally realized by using gyromagnetic materials (e.g., vanadium-doped calcium-iron-garnet) to construct a photonic crystal and applying a magnetic field [15]. Such metamaterials must be carefully designed and tend to have increased experimental complexity.

Since multipole topological insulators are the focus of this thesis, metamaterial systems that specifically implement these insulators are summarized below. In regards to the model-specific physics, multipole insulators preserve time-reversal symmetry, making the biggest experimental consideration the requirement of negative coupling between sites to realize a π-flux threading through each plaquette [9, 24, 25]. Negative coupling, in the context of a coupled-resonator system, refers to relationship between the polarity of two modes where they are coupled. Fig. 3.2 shows an the difference between negative and positive coupling using a p-orbital-like representation.

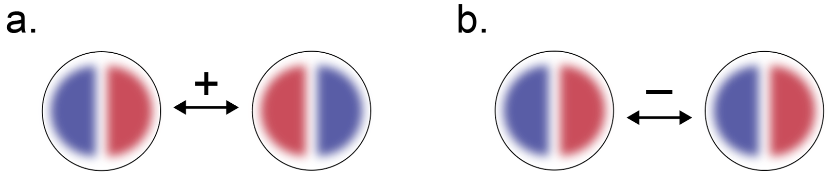

Figure 3.2: Illustration of negative and positive coupling. (a) Positive coupling between p-orbital-like modes. The phase relationship of the coupling region between both modes is positive (i.e., both regions have the same phase). **(b)** same as (a), but for negative coupling. The phase relationship of the coupling region is negative (i.e., the two regions have differing phases).

Multipole topological insulators have been successfully realized in acoustic [4, 5, 6], mechanic [3], and photonic [9, 10] coupled-resonator metamaterials. Each one of these implementations uses the same operating principle discussed in the first paragraph of Section 3.1.1. The primary distinction between different implementations is the type of resonant mode used.

The acoustic metamaterials use acoustic cavity resonances, and couple resonant modes through narrow channels [4, 5, 6]. Eigenmode simulations of the resonant modes are used to inform where the coupling channels should connect to each cavity (i.e., to implement positive/negative coupling correctly). These metamaterials are characterizing using a probe and sense procedure, where the probe is essentially a speaker and the detector is a microphone. These acoustic metamaterials can be fabricated using 3D printing techniques [4, 5, 6], giving this implementation the advantage of quick fabrication using in-house equipment. The equipment requirements to characterize these metamaterials are also minimal, making this approach cost-effective. However, these metamaterials tend to suffer from high material losses, resulting in low quality factor resonances compared to the higher frequency systems. This leads to broader resonance peaks, which can make the spectral band gap difficult to resolve.

Mechanical (phononic) metamaterials have also been used to construct a 2D quadrupole insulator [3]. This implementation used microfabrication techniques to create coupled mechanical resonators (each 5-mm by 5-mm by 0.364-mm-thick) from silicon plates. Each resonator is then connected to its neighbors by coupling beams. The resonant modes used in this system are the mechanical displacement eigenmodes, which were computed using commercial multiphysics simulation software [3]. This metamaterial was then characterized using a probe and sense scheme, where an ultrasound air transducer acts as the probe, and a laser interferometer measures the response [3]. This phononic metamaterial successfully implemented a quadrupole insulator and yielded high-quality results with clearly distinguishable band structure. However, it has some issues with mechanical resonators coupling to their next-nearest neighbors through second-order effects [3], causing the metamaterial to deviate from a nearest-neighbor only tight-binding Hamiltonian. Another disadvantage is that the mechanical resonators are relatively large in size, which limits the maximum system size that can be built. It is also important to note that this specific phononic metamaterial cannot be used to construct any 3D topological insulators, as the mechanical resonators would need to be completely redesigned to couple to six neighbors.

Photonic metamaterials have also been used to implement 2D quadrupole insulators. Specifically, coupled microwave resonators [9] and coupled integrated photonic resonators [10] have been used. The microwave approach used H-shaped microstrip transmission lines as the resonators, which were distorted to be physically close together to couple neighboring resonators with discrete capacitors. Negative coupling was achieved by connecting resonator arms with different polarities with a capacitor [9]. This metamaterial was characterized by taking one-port power reflection measurements with a vector network analyzer at each resonator in the array and then calculating the power absorptance. The integrated photonic approach used coupled ring resonators, which were designed to support a single mode near telecommunication wavelengths (1550 nm). Neighboring ring resonators were coupled together using linking rings, which interact by coupling through their evanescent fields [10]. Negative coupling was achieved by shifting the vertical alignment of the link rings, which changes the path length to induce a π-phase shift [10]. The corner modes were characterized by using waveguide couplers to measure the power absorption, and a high-sensitivity InGaAs camera was used to image the spatial distribution of absorption intensity [10].

Both the microwave and ring resonator systems were able to successfully observe the protected corner modes of a quadrupole insulator, proving that these metamaterials are suitable platforms for topological physics experiments. However, a disadvantage of both systems is that they are limited to 2D structures making direct implementation of a 3D octupole impossible. In terms of cost and ease of fabrication, the microwave system has an advantage. However, the photonic system is a more realistic platform for potential device design due to its compact size. Additional considerations include ease of measurement and required equipment. Characterizing the microwave system only requires a vector network analyzer [9], whereas the ring resonator system requires a tunable laser, photodetectors, an optical fiber network, and high-sensitivity imaging tools to spatially resolve the modes [10].

Electronic metamaterials that do not use a coupled-resonator framework have also been used to construct 2D and 3D multipole topological insulators [7, 8]. While these systems are not the focus of this thesis, it is worthwhile to briefly introduce their operating principle and identify some advantages and disadvantages. The construction of these electronic metamaterials relies on a mathematical equivalence between a tight-binding model Hamiltonian and the Laplacian of an electronic circuit and are often called "topolectric circuits" [7, 8, 51, 52]. The Laplacian is essentially a matrix representation of Kirchhoff's circuit laws and describes the connectivity of a circuit. When evaluated at a single frequency, the Laplacian is a square matrix that can be diagonalized to determine its eigenvalues/vectors. An advantage of the topolectric circuit approach is that the circuit directly implements the Hamiltonian of a topological insulator. However, significant disadvantage is that n^2 measurements of nodal voltages are required to populate the circuit Laplacian of a system with n-sites. Coupled-resonator approaches require a maximum of n measurements of a system with n-sites, which allows more direct access to the spectral density of states. The post-processing steps of the coupled-resonator approach are much simpler as a result, eliminating the need for matrix operations like inverses and diagonalization.

3.2 A circuit-based metamaterial

This section describes the design, construction, and characterization of the circuit-based metamaterial used to perform the partial dislocation experiments discussed in this thesis. Section 3.2.1 focuses on the implementation details and Section 3.2.2 focuses on the characterization procedure.

3.2.1 Construction

The circuit-based metamaterial was designed according to a coupled-resonator framework. Each resonator in this system is composed of two 200-pF capacitors and one 1-μH inductor arranged in a π-network, as shown in Fig. 3.3. This resonator network is commonly used to implement low-pass filters [53]. The resonance frequency is given by equation 3.1 [53], where the inductance (L) and capacitance (C) is defined according to Fig. 3.3.

$$\omega = \frac{2}{\sqrt{LC}} \tag{3.1}$$

The resonance frequency of each resonator was designed to be approximately 16 MHz (f_0 = 15.9 MHz, according to the analytical expression). However, the presence of capacitive loading (due to coupling network) causes

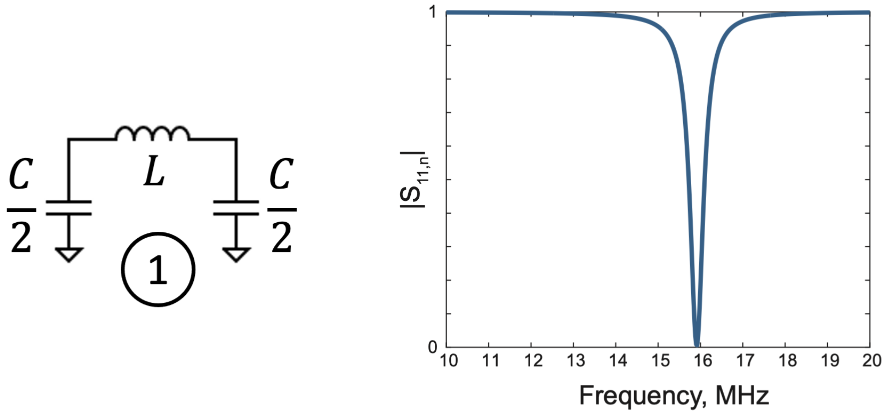

Figure 3.3: π-network resonator. Illustration of a single π-network LC resonator used in the circuit-based metamaterial, along with its power reflection response simulated in Advanced Design System (ADS). The following parameters were used for the simulation: $\frac{C}{2} = 200$ pF, L $= 1$ μH.

the resonance frequency of each resonator to shift downward in the measured metamaterial.

As discussed in Section 3.1.2, the multipole insulator models that are the focus of this thesis require a π-flux threading through each plaquette to open a band gap. This has been achieved in other implementations by using negative coupling; the same is done here. The main reason that the π-network resonators were selected for the circuit-based metamaterial is that they can implement negative coupling. This is not true for the "LC tank"-style resonators used in the SSH example in Section 3.1.1. This difference is the result of the π-network resonators having two nodes where they can be coupled rather than just one. As shown in Fig. 3.4, the phase relationship when two π-network resonators are coupled through the same nodes (e.g., node A to node A) is opposite of the phase relationship when two resonators are coupled through different nodes (e.g., node A to node B). For the purpose of this thesis, coupling two resonators from nodes with different labels (A to B) will be defined as negative coupling, and coupling two resonators from nodes with the same labels (A to A, or B to B) will be defined as positive coupling. This is a somewhat arbitrary choice, as defining the opposite relationships will yield the same observables. However, the primary reason that this convention was adopted was to minimize the trace length between the majority of connections in the system (which have positive coupling).

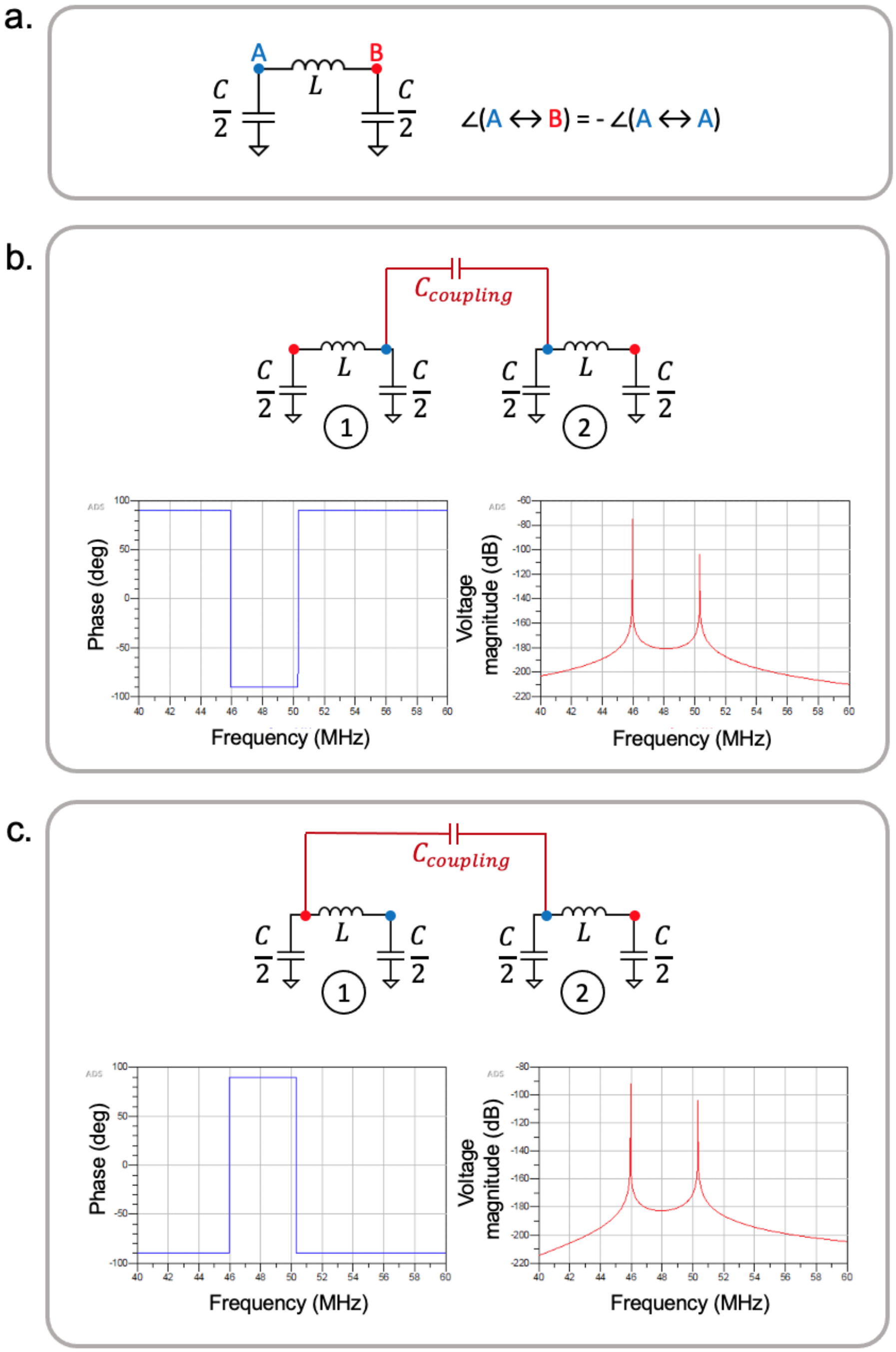

Figure 3.4: Negative coupling using π-network resonators. (a) Single π-network resonator with definition of nodes A (blue) and B (red). For (b) and (c), and throughout this thesis, the interior nodes of each unit cell are defined as the "A" nodes. **(b)** Two π-network resonators coupled at different nodes (B for resonator 1 and A for resonator 2) with resulting magnitude and phase response **(c)** same as (b), but for both resonators coupled at node A

Since the multipole models that are the focus of this thesis have a highly periodic structure with nearest-neighbor coupling, a modular approach was taken to design the circuit implementation. The tight-binding model of quadrupole unit cell was used as a basic building block for this design. Thus, each modular board was designed to contain four resonators to reproduce the four degrees of freedom per quadrupole unit cell in Fig. 1.4b. These modular circuit boards were also designed to be physically reconfigured (via solder jumper pads or direct wiring) to realize both quadrupole and octupole unit cells. An octupole unit cell can be constructed using two modular boards. Annotated pictures of the modular circuit boards used to construct quadrupole and octupole unit cells are shown in Fig. 3.5.

The modular circuit boards were designed such that each resonator can support up to six connections (four in-plane and two out-of-plane), which were enabled by solder jumpers. Each in-plane connection has the option of positive or negative coupling, which corresponds to a connection at the inner or outer node (with respect to the center of the board), respectively. In addition, each possible connection have the option of strong or weak coupling, which is again controlled by solder jumpers. An illustration of these solder jumper connections are shown in Fig. 3.6. Each in-plane connection has all of the coupling options depicted in Fig. 3.6; the out-of-plane connections have the same coupling options with the exception of negative coupling. Strong coupling corresponds to connecting a 100 pF capacitor between two resonators in series, and weak coupling corresponds to connecting a 10 pF capacitor. Shorting two resonators corresponds to directly wiring them together. This connection was not used explicitly to implement the multipole models. However, there is a redundancy in each board-to-board connection (e.g., the coupling can be defined on board 1 and on board 2), which makes the short option a necessity. The solder jumpers are “enabled” by soldering together the two jumper pads.

The option to add loading capacitors to each resonator was also incorporated into the design of the modular circuit boards. These loading capacitors effectively introduce an on-site potential to the resonator they are appended to. The placement of the optional loading capacitor relative to a single resonator is shown in Fig. 3.7. These loading elements were designed to affect each resonator in a symmetric way (i.e., as opposed to connecting a loading element to single node of the resonator).

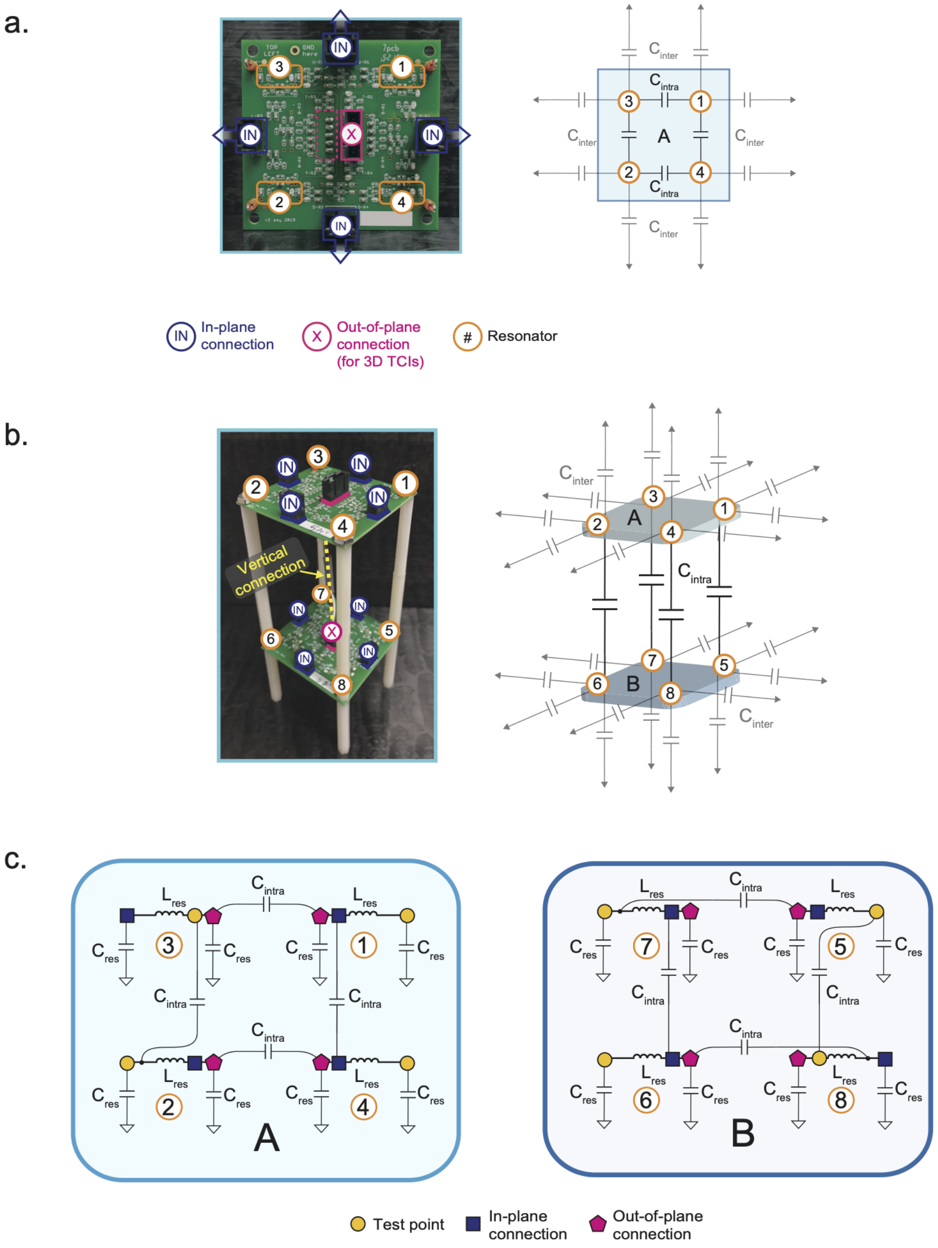

Figure 3.5: Details of circuit implementation. **(a)** Photo of quadrupole TCI unit cell and illustration of inter-cell connectivity **(b)** same as (a) but for octupole TCI **(c)** Schematic of circuit used to realize a single octupole TCI unit cell with 8 sites. The sub-units A and B each correspond to one modular circuit board. Only the A sub-units were used to realize the 2D quadrupole TCI. The nodes used as measurement test points are labeled with yellow circles. In-plane connections to neighboring circuit boards were made at the nodes labeled by the green squares. Out-of-plane connections were made at the nodes closest to the center of each circuit board and are labeled with purple pentagons. The component values used were: C_{res} = 200 pF, L_{res} = 1 μF, C_{intra} = 10 pF, and C_{inter} = 100 pF

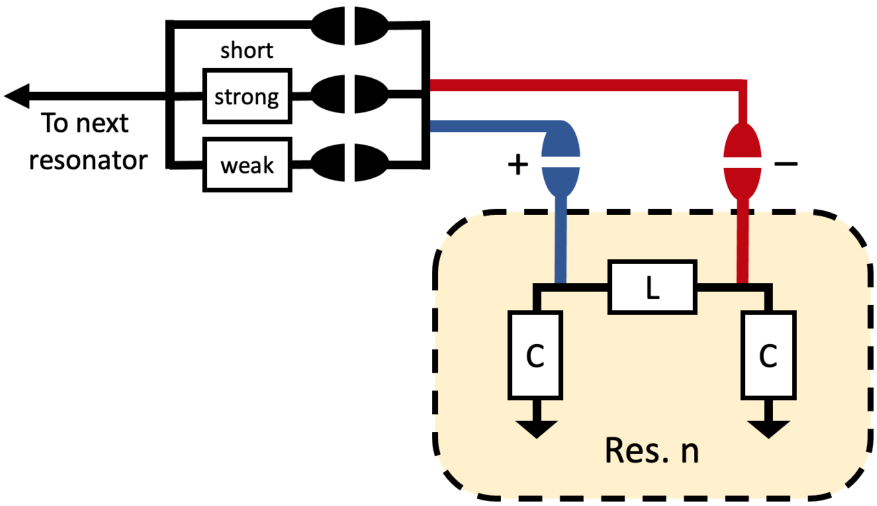

Figure 3.6: Solder jumpers. Illustration of a solder jumper connections to neighboring in-plane resonator. For each resonator, the depicted connections are repeated along both the $\hat{x}$ and $\hat{y}$ directions, allowing the experimentalist to define how each resonator is connected to its four nearest in-plane neighbors.

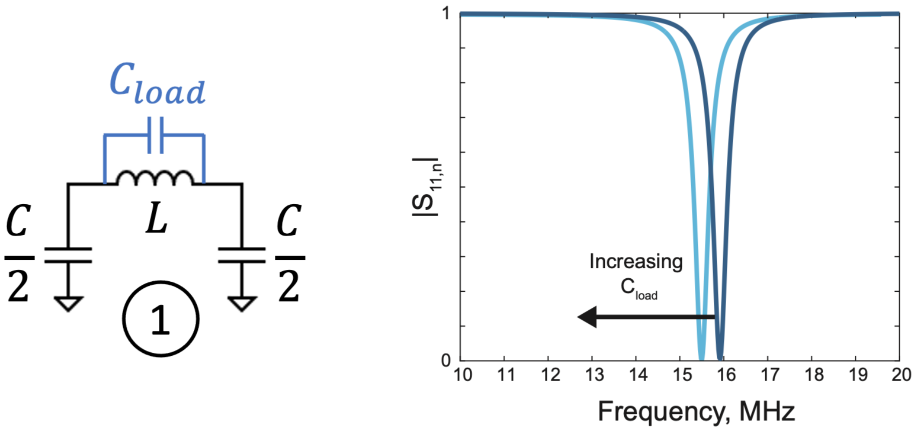

Figure 3.7: Loading capacitor. Illustration of single π-network resonator with loading capacitor. The addition of a loading capacitor shifts the resonance frequency downward. The downward frequency shift increases as a function of loading capacitance– this effect is depicted by the lighter blue —S_{11}— trace.

All of the circuit simulations for the quadrupole and octupole TCIs were performed in Advanced Design System (ADS). These simulations were used to optimize the design of the quadrupole and octupole TCIs as well as determine component values. A resonance frequency of approximately 16 MHz was selected for the following reasons: (i) the frequency is low enough relative to the size of a normal printed circuit board (PCB) that high-frequency effects like transmission line impedance could be neglected, (ii) the component values necessary to realize this resonance frequency were readily available with reasonable tolerances, ± 5-10% variation, (iii) inductors with quality factors of 50 or higher within the same frequency range could be purchased. Additional design considerations include that the capacitors which implement strong coupling should not exceed the capacitance value of resonator capacitors, and that the ratio of C_{inter}:C_{intra} should be sufficiently large to open up a spectral band gap. For this implementation, C_{inter}:C_{intra} was chosen to be 10:1. These considerations informed the selection of the final component values in Table 3.1. These component definitions correspond to the labeling in Fig. 3.5.

Table 3.1: Component Values for Modular PCB

Component	**Nominal value**	**Tolerance**
C_{res}	200 pF	±5%
L_{res}	1 μH	±10%
C_{intra}	10 pF	±5%
C_{inter}	100 pF	±5%

The modular circuit boards were designed using Autodesk EAGLE and were fabricated by a commercial PCB manufacturing service on FR4 substrate with 1-oz. copper. Each board measures to be 0.063-inches thick and approximately 2.5-inches x 2.6-inches in area. All of the passive components were selected to have 0603 (metric) package sizes. A total of 54 modular circuit boards were needed to construct the largest measured system, a 3 × 3 × 3 octupole TCI. Since so many circuit boards were needed, an in-house assembly service was used to populate all of the passive components on each board. Larger components like the plastic connectors for board-to-board wiring and test points were manually soldered. The PCB layout for a single modular board is shown in Fig. 3.8. An annotated version of the PCB layout is also presented in Fig. 3.9. Since the PCB is essentially divided into four repetitive quadrants (one for each resonator), a single quadrant is zoomed in on and explained. In Fig. 3.9, each component and solder jumper is identified and each label is explained. To better understand how the modular PCBs were used to implement the multipole TCIs, the components and solder jumpers necessary to realize quadrupole and octupole unit cells are shown in Fig. 3.10 and Fig. 3.11, respectively. As a final example, the layout of a 2 × 2 quadrupole is provided in Fig. 3.12 to illustrate how the modular PCBs can be wired together to form arrays.

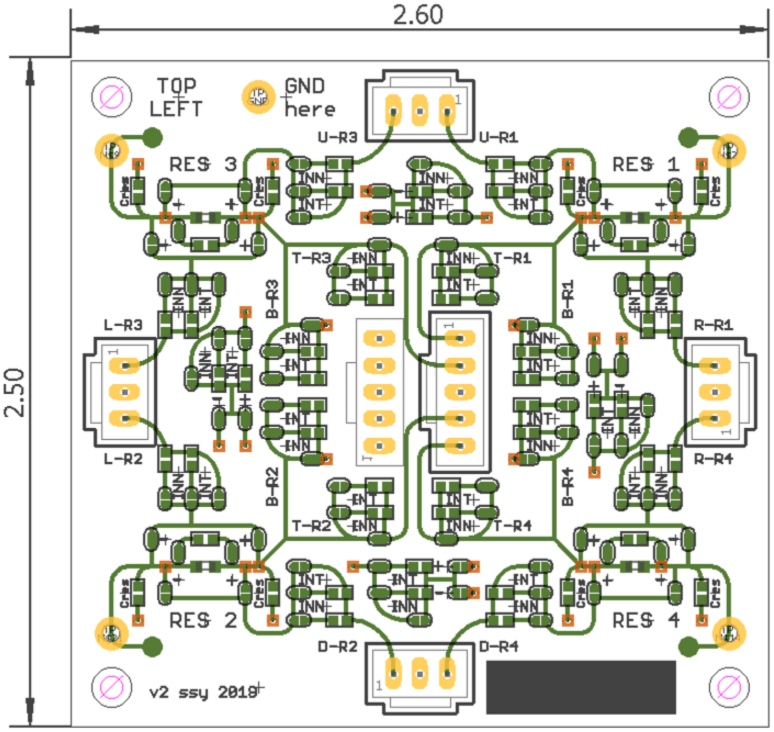

Figure 3.8: PCB layout. Layout of a single modular circuit board used to construct the circuit-based metamaterials used in this thesis. Each quadrant contains a single π-network LC resonator. Each resonator is connected by a network of capacitors and solder jumpers that allow different coupling configurations to be defined by the experimentalist.

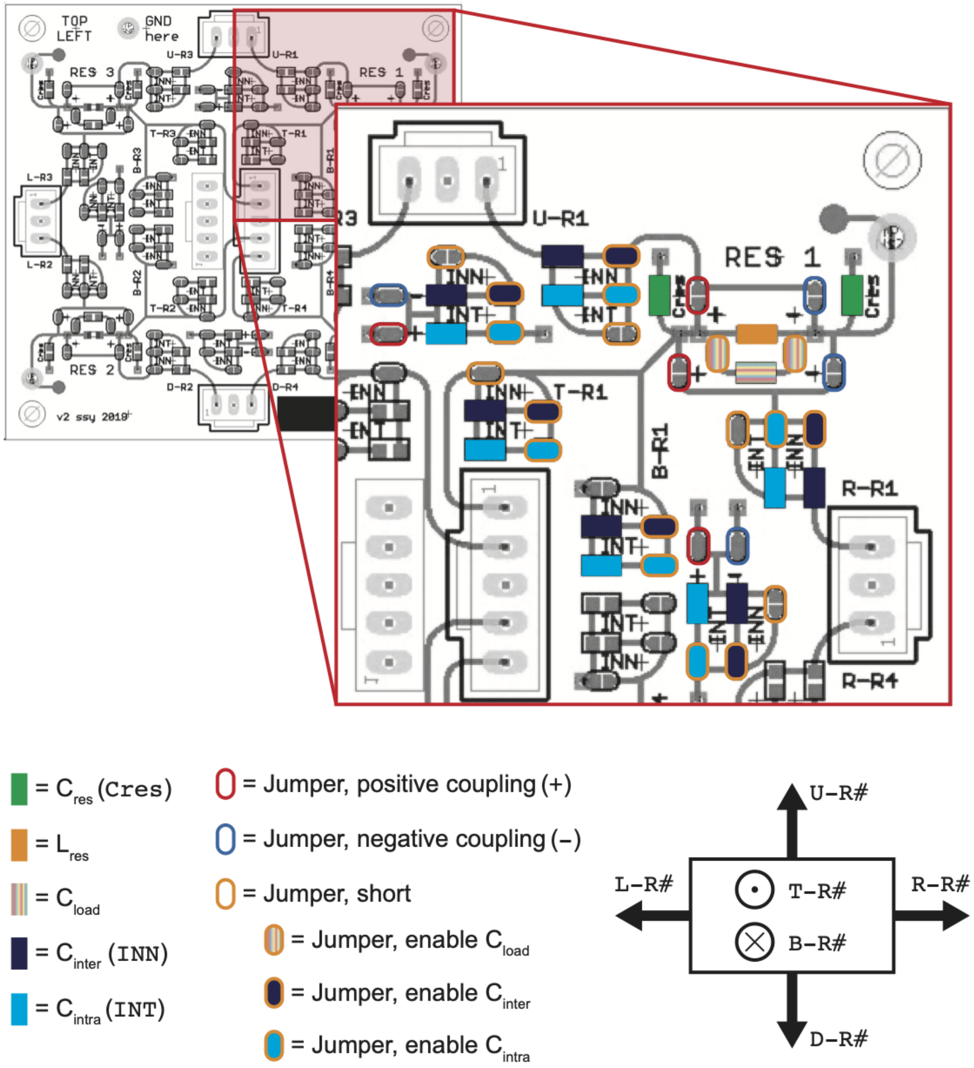

Figure 3.9: Annotated PCB layout. Explanation of a single quadrant of the modular PCB. All components and solder jumpers are identified, and their functions indicated in the key at the bottom of the figure. Surface mount components are indicated by solid rectangles and jumpers are indicated by ovals. Each resonator supports up to six connections which are labeled using the notation [D-R#], where D is a single letter indicating the direction, and # indicates which resonator the direction is referenced from. The design of the modular circuit board is divided into four repetitive quadrants, so understanding the connectivity of a single quadrant is sufficient to interpret the remaining three quadrants.

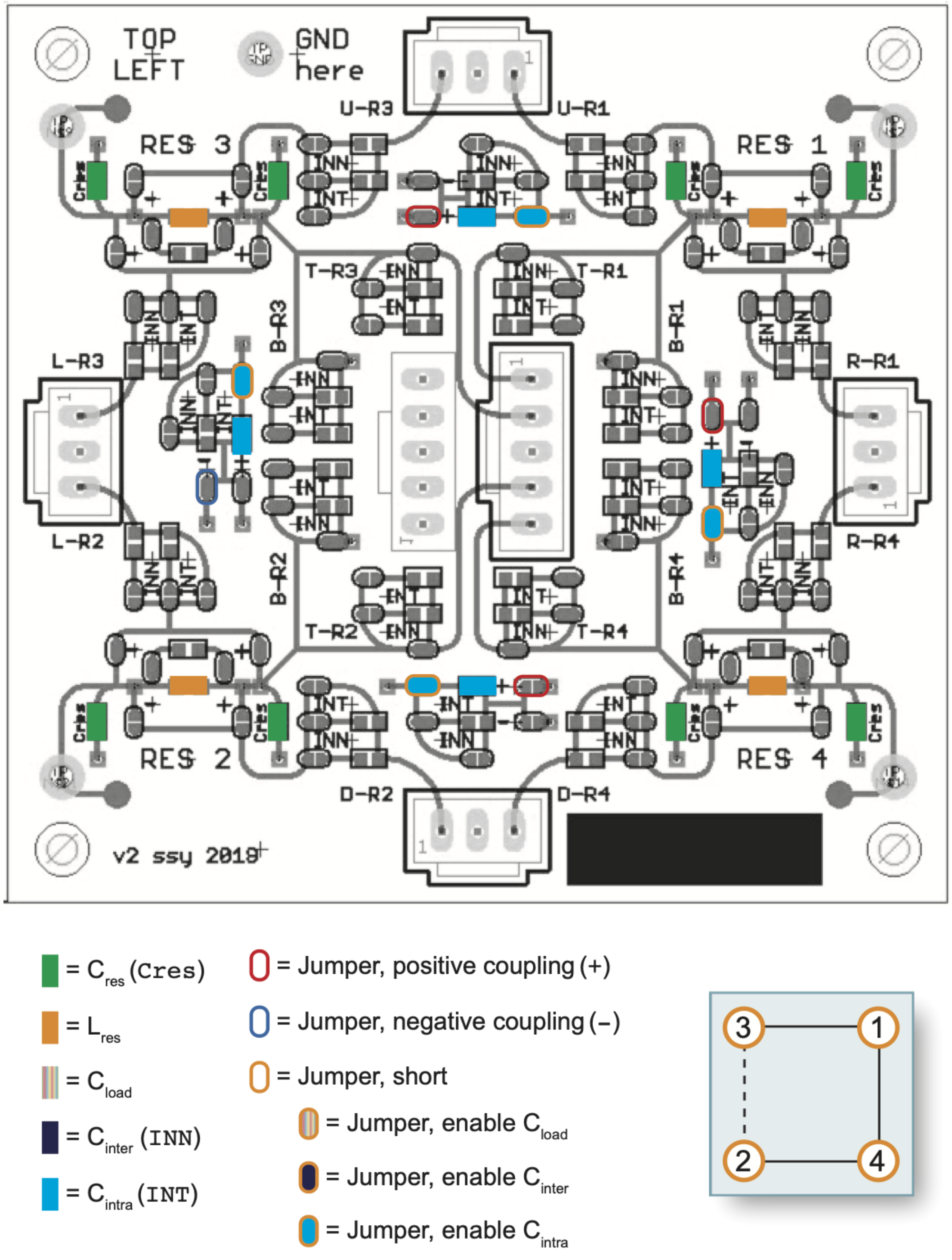

Figure 3.10: PCB layout that implements a unit cell of a quadrupole TCI. The minimum necessary components and connections needed to realize a single unit cell of a quadrupole TCI are identified on the modular PCB layout.

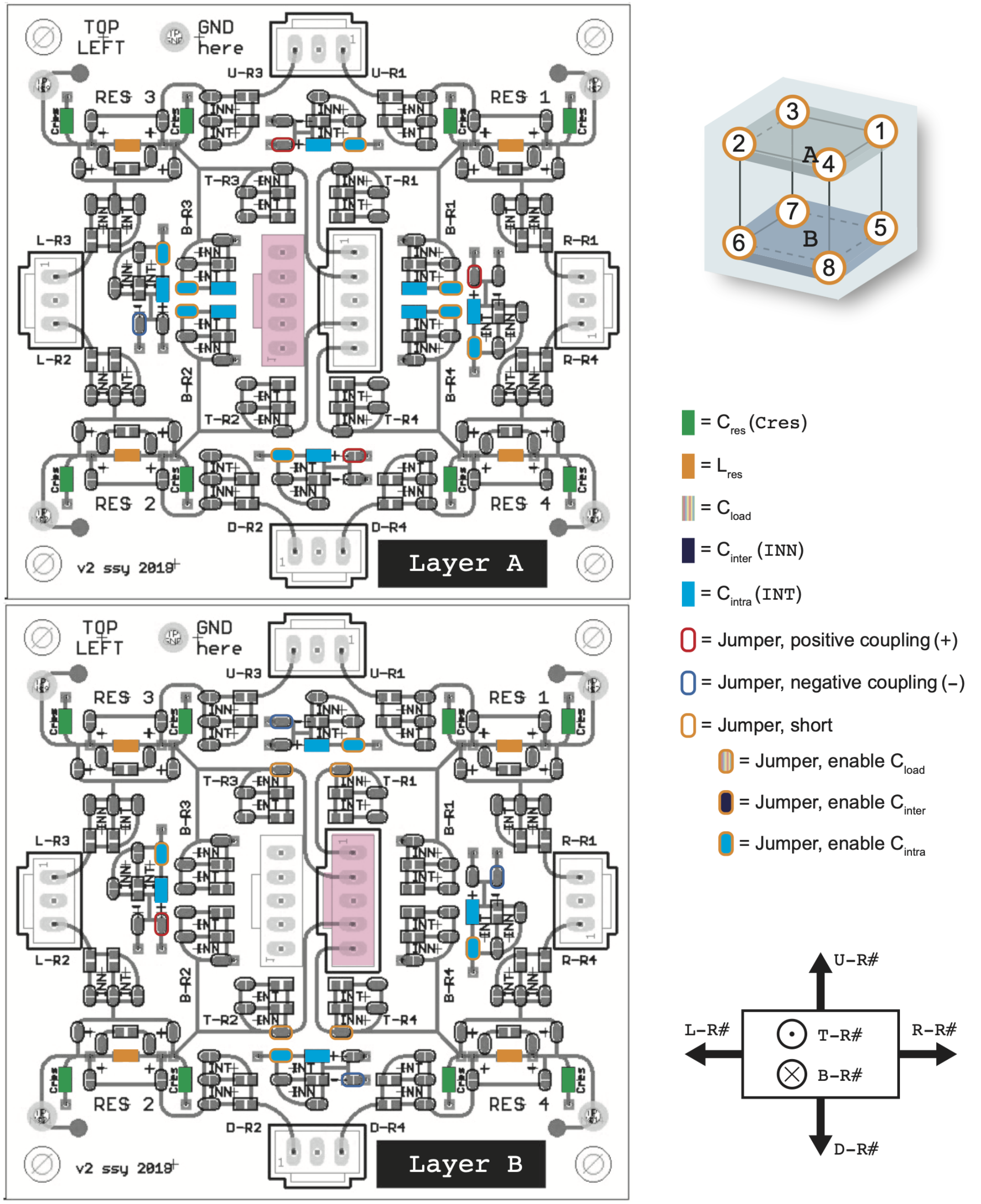

Figure 3.11: PCB layout that implements a unit cell of an octupole TCI. The minimum necessary components and connections needed to realize a single unit cell of an octupole TCI are identified on the modular PCB layout. Two modular PCBs are needed per unit cell and must be directly wired together; this connection is indicated by the semi-transparent pink boxes.

The boards themselves were designed to be connected together by wires to form arrays. In-plane connections between boards were made using 3-strand wires, consisting of two wires leading to the closest resonators and a ground wire. Out-of-plane connections between boards were made using 5-strand wires, consisting of one wire per resonator and a ground wire. A common ground was established throughout the metamaterial by ensuring that every board-to-board connection included a grounded wire. Fig. 3.13 shows photos of the assembled 2D quadrupole and 3D octupole insulators. The 3-strand and 5-strand wires used in these experiments were made by hand, which in retrospect was not a good design decision. The process to fabricate each cable was tedious, as each individual wire needed to be stripped, equipped with a metal crimp housing, and inserted into a plastic plug. In total, 72 3-strand wires and 45 5-strand wires were necessary to construct the $3 \times 3 \times 3$ octupole TCI. To put this effort into perspective, the process of stripping each wire and applying a crimp housing had to be repeated over 880 times to construct these systems. Thus, it is advised that fully fabricated wires and the appropriate receptacles be purchased rather than hand-assembled for any future work.

The circuit implementation was also designed to allow periodic boundary conditions to be enforced. These configurations were achieved through direct wiring, as shown in Fig. 3.14. It is important to note that the coupling connecting the top of the system to the bottom must be appropriately defined. In practice, this means disassembling either the top or bottom row (layer) of the 2D (3D) system and enabling the solder jumpers that implement strong coupling. The simplicity of implementing periodic boundary conditions can be seen as an advantage of a low-frequency circuit approach, as alternative metamaterial systems like coupled microwave resonators [9, 39, 28] or coupled acoustic cavities [5, 6] do not have this functionality.

The modular circuit-based metamaterial also has the advantage of being quick to simulate, design, and fabricate. It is also facile to construct 3D systems, which is not true for some other metamaterial platforms (e.g., coupled microstrip resonators, coupled photonic resonators). Disadvantages of the circuit-based metamaterial platform include reliance on commercial off-the-shelf components, and low quality factor resonances compared to microwave and photonic metamaterials.

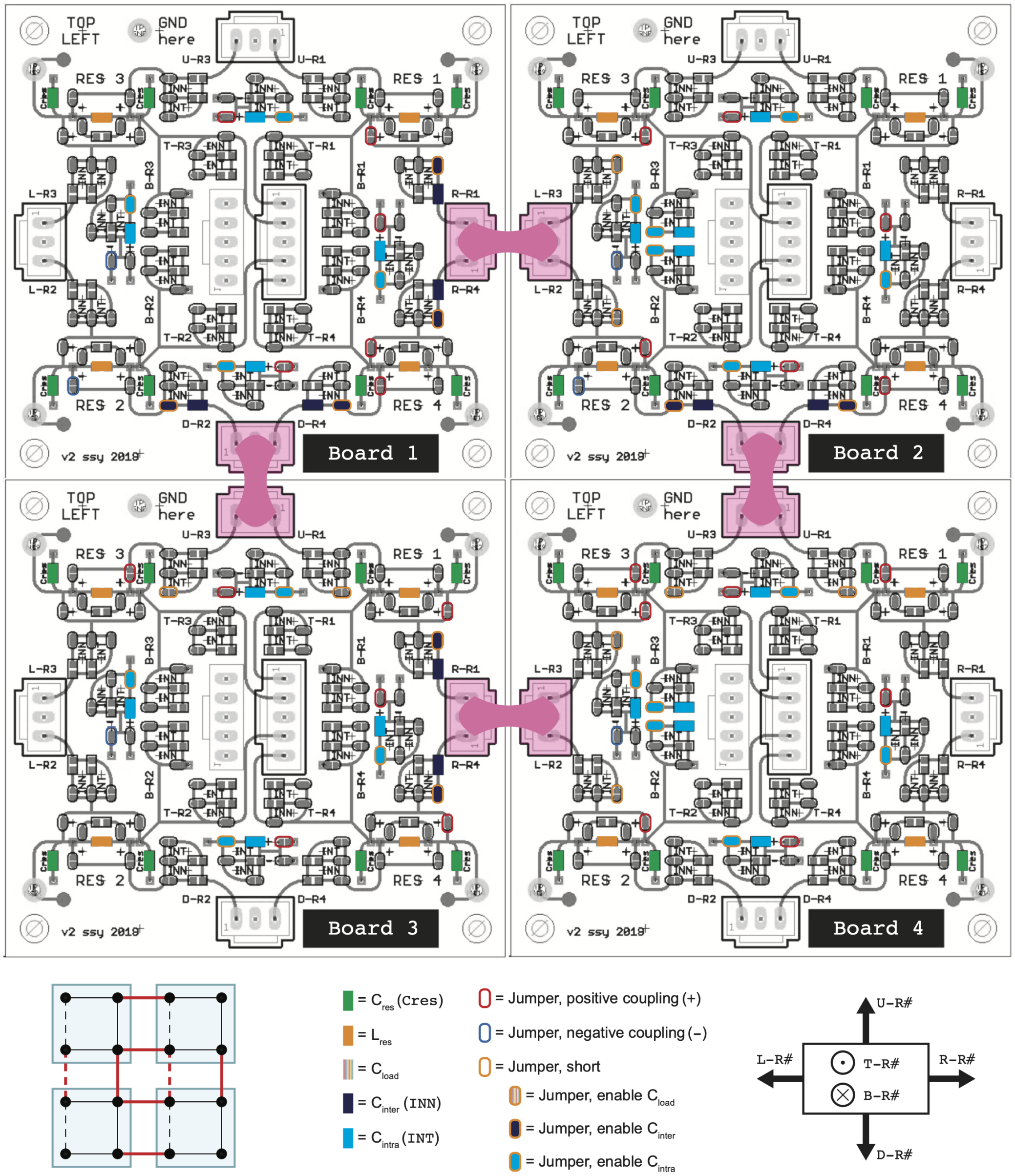

Figure 3.12: PCB layout that implements a 2 × 2 octupole TCI. The minimum necessary components and connections needed to realize a 2 × 2 quadrupole TCI are identified on the modular PCB layout. Four modular PCBs must be directly wired together to form an array; these connections are indicated by the semi-transparent pink boxes and bridges.

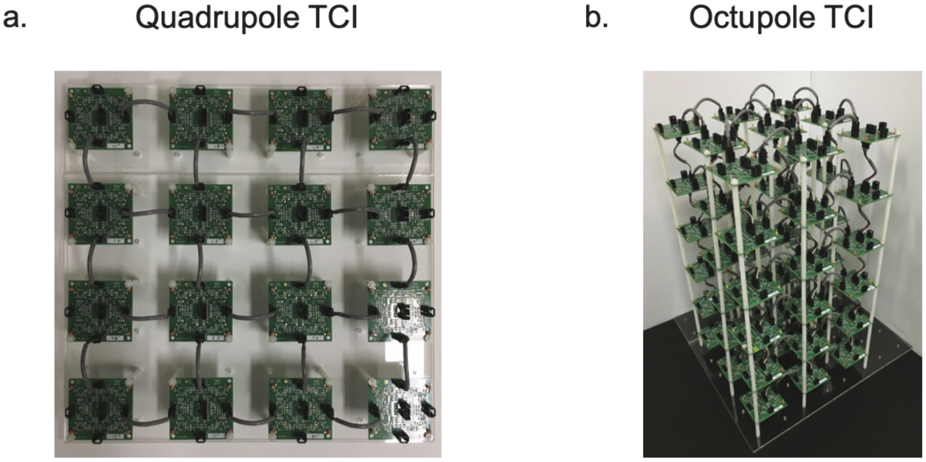

Figure 3.13: Photos of assembled metamaterials. (a) Fully assembled 4 × 4 2D quadrupole TCI **(b)** Fully assembled 3 × 3 × 3 octupole TCI

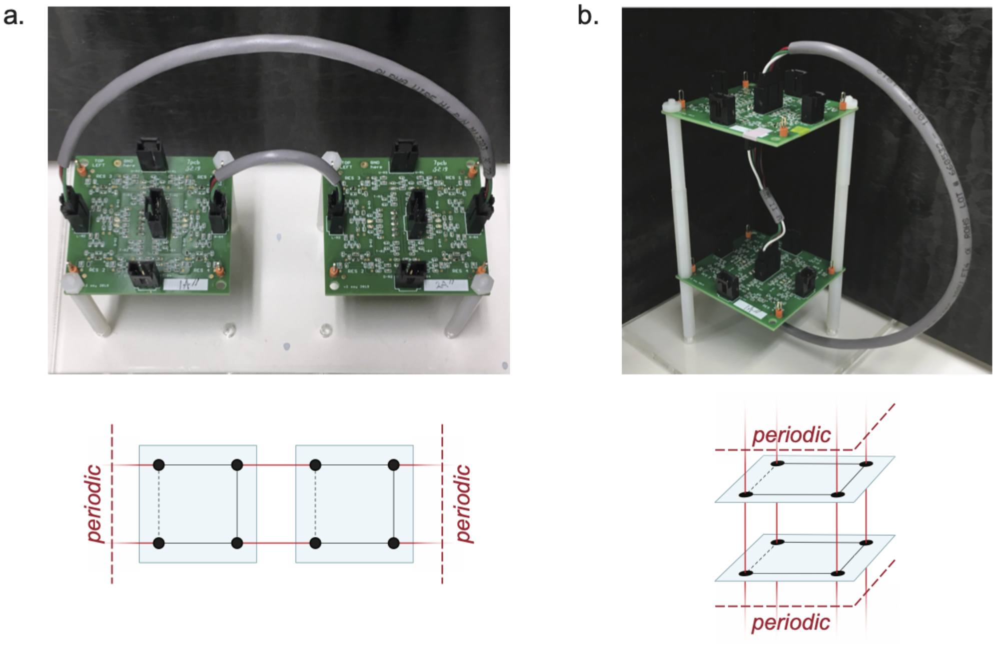

Figure 3.14: Implementing periodic boundary conditions. (a) Example of in-plane and **(b)** out-of-plane periodic boundary conditions using two four-site unit cells. Periodicity is enforced by physically wiring the two unit cells together.

3.2.2 Characterization

One-port power reflection (S_{11}) measurements were taken at each resonator using a vector network analyzer (Keysight E5063A) to obtain the spectral density of states (DOS), similar to the procedure in [9, 28, 39]. The probe used for these measurements was a 50-Ω SMA connector that was locally grounded to the device under test and terminated with a 24-pF capacitor. An example of this measurement and photo of the test sites is shown in Fig. 3.15. Next, the power absorptance (A_n) was calculated for each n^{th} resonator according to equation 3.2; the power absorptance is defined as the ratio of absorbed to incident power.

$$A_n(f) = 1 - |S_{11,n}(f)^2| \tag{3.2}$$

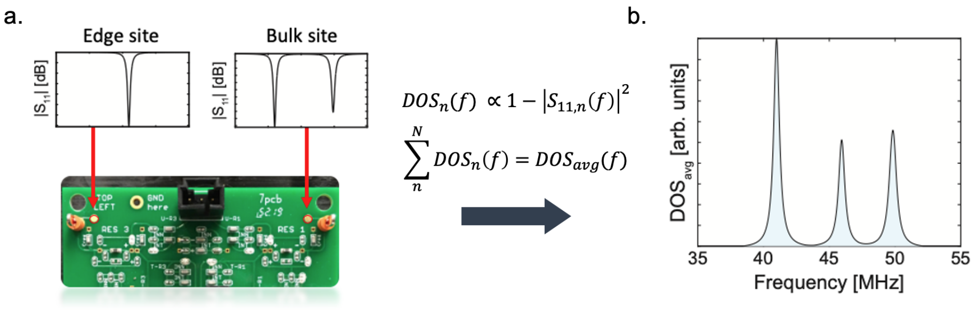

Figure 3.15: Example measurement of two sites. (a) Examples of $|S_{11,n}|$ data and photo identifying the measurement test pads (circled in red) on a modular circuit board. **(b)** Example of the computed band structure, DOS_{avg}. This specific data set is from a simulation of the circuit implementation of an SSH chain (Section 3.1.1) performed using Keysight Advanced Design System (ADS). The resonance frequency of each LC-resonator in this example was designed to be 50 MHz.

From the power absorptance (A_n), the local DOS ($DOS_n(f)$) of each n^{th} resonator was calculated according to equation 3.3.

$$DOS_n(f) = \frac{A_n(f)}{f^2} \tag{3.3}$$

This expression accounts for stronger coupling to our capacitive probe at higher frequencies. Since each resonator supports a single mode within the measured spectrum, $DOS_n(f)$ is normalized such that the local DOS measured at each individual resonator across all bands integrates to 1 (equation 3.4).

$$\int DOS_n(f)\,df = 1 \tag{3.4}$$

In practice, this was achieved by evaluating the matrix operation in equation 3.5, where DOS_n is an ordered column vector containing the computed local DOS of a single resonator over the measured spectral range, $f_1 - f_2$.

$$DOS_n(f) = \frac{DOS_n(f)}{\sum\limits_{f=f_1}^{f_2} DOS_n(f)} \tag{3.5}$$

After the local DOS of each resonator was properly normalized, the spectral band structure of the entire system (DOS_{avg}) was computed according to equation 3.6.

$$DOS_{avg}(f) = \sum_{n=1}^{N} DOS_n(f) \tag{3.6}$$

It follows that for a N-resonator system, there are N modes in total (equation 3.7).

$$\int DOS_{avg}(f)\,df = N \tag{3.7}$$

This measurement procedure was used to characterize all of the systems discussed in this thesis and is based upon the techniques described in [9, 28, 39]. A disadvantage of this method is that there can be some variation in the measured results depending on where each resonator is probed. This variation is more pronounced in systems with distributed elements (e.g., microwave resonators), as the wavelengths associated with the spectral range of interest is of the same order of magnitude as feature sizes in the system. In the lumped-element system presented in this thesis, measurement variation can be observed when the resonators are probed from different nodes (e.g., node A vs. node B in Fig. 3.4). To alleviate this issue, dedicated test pads connected to node B were included in the PCB design. However, the necessity of negative coupling to implement these models limited the effectiveness of this solution.

In general, each resonator should be probed at a node that is minimally coupled to other resonators. E.g., if a π-network resonator is coupled to three other resonators at its A-node, then its response should be probed at its B-node. The implementation of negative coupling complicates this because some resonators are coupled more strongly to the rest of the system at their B-nodes. The current working solution to this issue is to tag the resonators that must be probed at their A-nodes (i.e., labeled with a small piece of tape), and measure any unlabeled nodes at their dedicated test pads. Better solutions include adding an additional test pad to each resonator so that there is one for each node, or using a single test pad but adding solder jumpers that can select which node the test pad is connected to. The advantage of having two test pads per resonator is that either node can be measured at any time without modifications to any of the PCBs; however, this may lead to experimental error if the test pads are not labeled clearly. Using solder jumpers eliminates the concern of measuring the wrong test pad, but does so at the expense of taking the time to solder the appropriate jumper for each resonator.

CHAPTER 4

EXPERIMENTAL RESULTS

This chapter presents the experimental results of the initial metamaterial characterization and the partial dislocation defect study. Section 4.1 provides measurements that verify the multipole behavior of the metamaterials, and Section 4.2 focuses on the partial dislocation experiments.

4.1 Multipole topological insulators

As discussed in Section 1.1.3, multipole insulators are classified as higher-order topological insulators. As a result, 0D bound states are expected to be localized at the higher-order boundaries (i.e., corners) of these insulators when their unit cells support quantized multipole moments [24, 25].

4.1.1 Quadrupole insulator

Before the partial dislocation defect experiments were performed, a 2D quadrupole insulator with open boundary conditions was constructed. According to the tight-binding model for this insulator [24, 25], 0D topologically protected modes should be localized at the corners of the material. The local DOS was measured at each site in the metamaterial and is shown in Fig. 4.1. The local DOS measurements were then averaged over each feature group of resonators (e.g., corners, edges, bulk) to produce the result shown in Fig. 4.5a. It should be noted that the corner modes were tuned to appear within a spectrally bare region of the band structure by adding loading capacitors to the resonators that they are spatially localized to. The nominal values of the loading capacitors used to achieve this are listed in Table 4.1 and follow the numbering of the inset local DOS plots in Fig. 4.2. Fig. 4.5b was obtained by selecting the spectral range (SR) that corresponds to where the corner sites are dominantly excited– in this measurement that range is 13.1 - 13.4 MHz– and plotting the spatial distribution of the mode density at each site over that range. The mode density refers to the magnitude of excitation (at a given site) over a specified range of energy/frequency. From this spatial mapping of mode density, it can be concluded that the corner modes are spatially localized at the corner resonators.

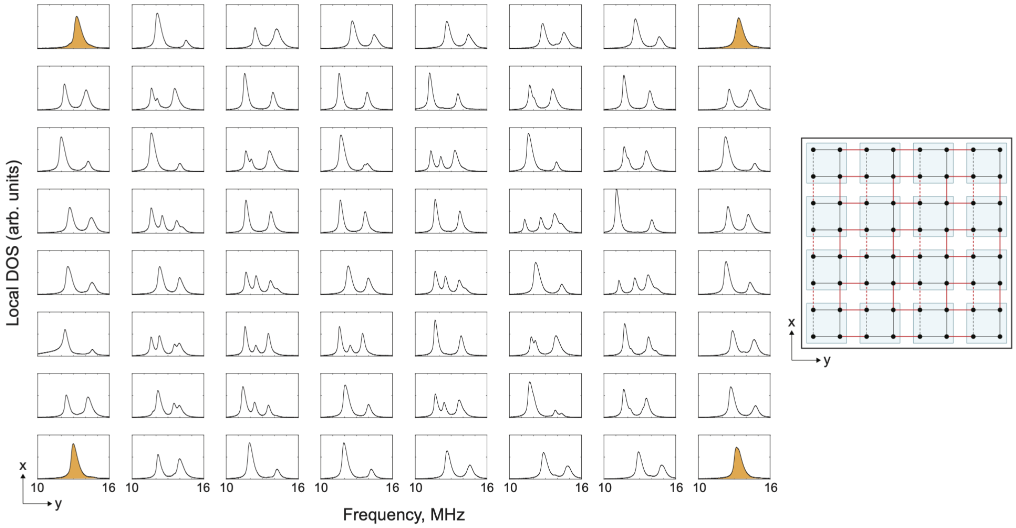

Figure 4.1: Measured local DOS at each site for a 4 × 4 unit-cell quadrupole TCI. These measurements correspond to Fig. 4.2. The organization of the grid follows the topology on the right, where the red (black) lines denote strong (weak) coupling, and the dashed lines denote negative coupling. In the DOS measurements, sites that are anticipated to host a corner mode or bound state are highlighted in yellow.

In Fig. 4.1, the local DOS of the sites anticipated to host 0D corner modes are highlighted in yellow. By inspection, the local DOS at these sites are different than the local DOS at all other sites in the array because they have a single spectral peak. This indicates that the modes supported by these resonators composing these sites are spectrally gapless. The absence of additional peaks indicates that the mode localized at that site cannot tunnel to other bands and is thus spectrally isolated. This specification along with the spatial distribution of the mode density in Fig. 4.5 leads to the conclusion that the highlighted modes are both spatially and spectrally isolated to single sites in the lattice.

It can be noted that there is some band gap misalignment between resonators that support different spectral features, e.g. resonators at the edges

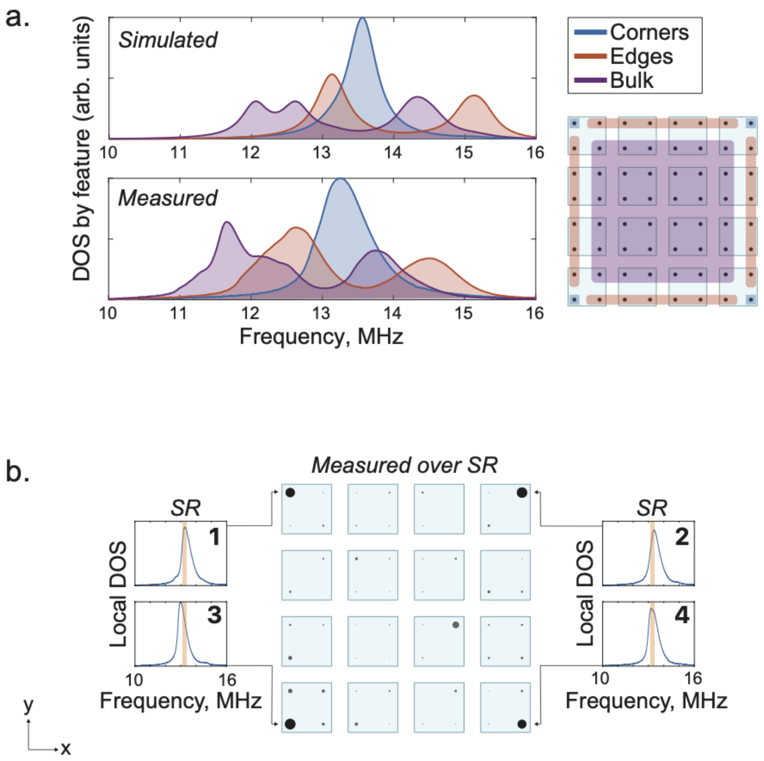

Figure 4.2: Quadrupole TCI density of states (DOS). (a) Measured DOS averaged over sites that lie on the corresponding feature groupings for the quadrupole TCI. **(b)** Spatial map of the mode density at each site over the highlighted spectral range (SR: 13.1 - 13.4 MHz), which corresponds to where the corners have the highest mode density and where the edge and bulk spectra are gapped. Each site is represented as a circle with radius proportional to the local mode density.

of our material compared to resonators in the bulk. This misalignment is a consequence of both uncompensated loading effects and disorder in the system. Loading effects in the metamaterial can be understood by considering the systematic variation in the local capacitive load at different resonators based on their connectivity. For example, in the quadrupole TCI a bulk resonator experiences a greater capacitive load than an edge resonator because it is strongly coupled to a greater number of neighbors. This increased capacitive loading cause the bulk bands to shift downward in frequency, relative to the edge bands. The implementation of negative coupling also causes a systemic asymmetry of the positive and negative coupling rates. Additionally, the manufacturing tolerances of the discrete components used to construct the resonators creates inherent disorder in the system.

Table 4.1: Loading Capacitor Values for Quadrupole TCI Corner Modes

Component	Nominal value	Tolerance
C_1	24 pF	±5%
C_2	5.6 pF	±0.25 pF
C_3	24 pF	±5%
C_4	24 pF	±5%

4.1.2 Octupole insulator

For the same reasons discussed in the last section, a 3D octupole insulator with open boundary conditions was also constructed and measured. Like the quadrupole insulator, topologically protected 0D modes were anticipated to be localized at the corners of this metamaterial. The same measurement procedure was then applied to characterize the band structure (i.e., DOS): first the local DOS was measured at each site (Fig. 4.3), then those measurements were averaged over the different features of the material (Fig. 4.9a), and finally the spatial mapping of mode density was obtained to verify the localization of the corner modes (Fig. 4.9b).

It can be observed from Fig. 4.3 and Fig. 4.4a that the corner sites are the only sites in the array that have single-peak spectra. This indicates that the corner sites are spectrally isolated from the other sites in the metamaterial. While it is difficult to see in Fig. 4.9a, the hinge, surface, and bulk sites all have multiple spectral peaks, which implies a spectrally gapped band structure. These modes can be resolved more easily by looking at the local DOS in Fig. 4.3. The spatial mapping of mode density (over the SR of 12.75 - 13.05 MHz) in Fig. 4.9b shows that the corner modes are also spatially localized at the corner sites. These modes were tuned to appear within a spectrally bare region of the band structure by adding loading capacitors to the resonators that they are spatially localized to. The nominal values of the loading capacitors used to achieve this are listed in Table 4.2. This Table follows the numbering of the inset local DOS plots in Fig. 4.4. It can also be observed that there are some bulk and hinge modes that are also excited over the same SR. These excitations are the result of the uncompensated loading effects and disorder discussed in the previous section.

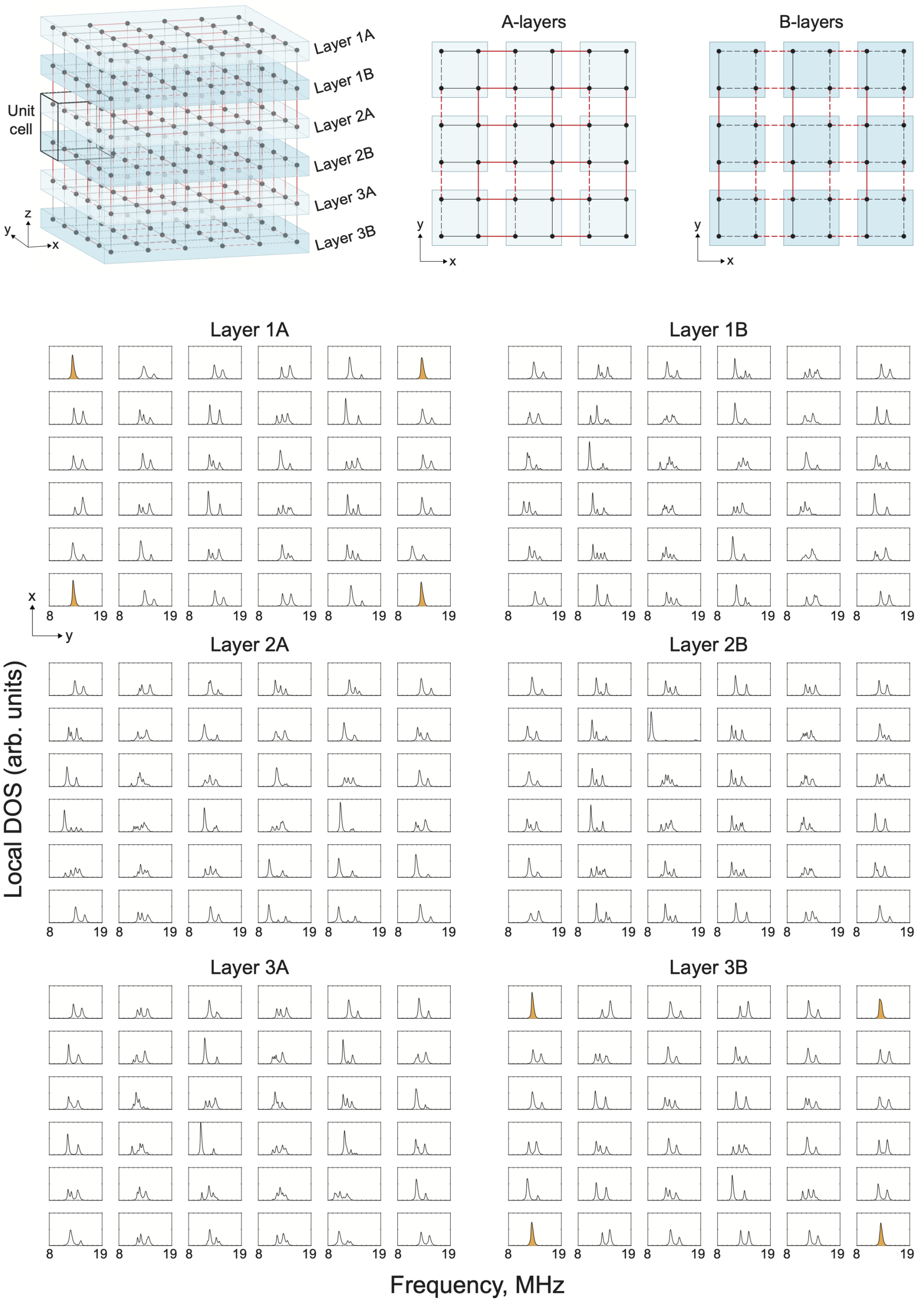

Figure 4.3: Measured local DOS at each site for a $3 \times 3 \times 3$ unit-cell octupole TCI with open boundaries. These measurements correspond to Fig. 4.4. The organization of the grid follows the topology on the right, the red (black) lines denote strong (weak) coupling, and the dashed lines denote negative coupling. In the DOS measurements, sites that are anticipated to host a corner mode or bound state are highlighted in yellow.

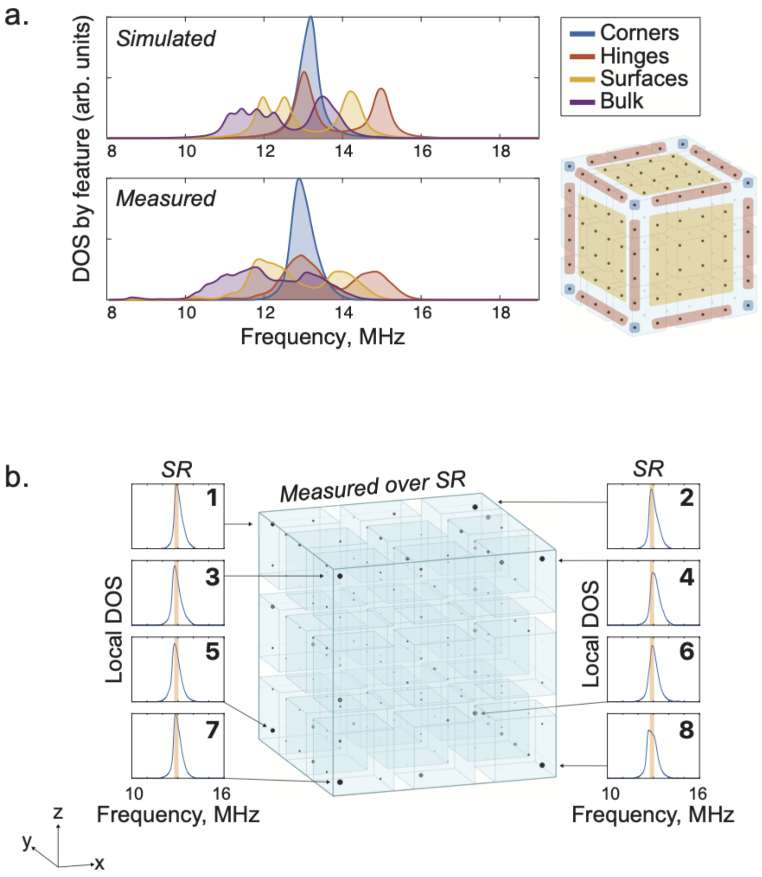

Figure 4.4: Octupole insulator density of states (DOS). (a) Measurements of DOS for the octupole TCI averaged by feature grouping **(b)** Mode density at each site in the octupole TCI excited over the highlighted spectral range (SR: 12.75 MHz - 13.05 MHz).

Table 4.2: Loading Capacitor Values for Octupole TCI Corner Modes

Component	Nominal value	Tolerance
C_1	24 pF	±5%
C_2	5.6 pF	±0.25 pF
C_3	24 pF	±5%
C_4	24 pF	±5%
C_5	24 pF	±5%
C_6	8.2 pF	±0.25 pF
C_7	24 pF	±5%
C_8	24 pF	±5%

4.2 Bound states at partial dislocation defects

4.2.1 Partial dislocations in a quadrupole TCI

This section explores the results of inserting a partial dislocation defect into the 2D quadrupolar TCI (Fig. 4.5a). To begin this procedure, a periodic boundary condition was enforced along the y-direction to gap out the outer corner modes and hence minimize boundary effects. A partial dislocation composed of 3×12 quadrupolar unit cells was then introduced along the x-axis. As discussed earlier, topological bound modes are anticipated to be localized near the higher-order boundaries of the phase boundary formed by the inclusion of the partial dislocation.

However, the exact spatial distribution of these modes depends on how the boundaries of the partial dislocation are coupled to the original lattice. The bound state can then be spatially localized to a single site by locally deforming the inter-site connectivity at the higher-order boundaries of the partial dislocation (see Fig. 4.8). This deformation does not disturb the protective reflection symmetry of the inserted partial dislocation, nor does it destroy the topological phase boundary, so the global properties of the structure remain unchanged. Experimental measurements shown in Fig. 4.5a confirm that the bound states are both spectrally gapless and are spatially localized at the higher-order boundaries of the partial dislocation. This can be further confirmed by inspecting the local DOS at each site in Fig. 4.6. In this figure, the spectra of the bound states are highlighted in yellow and exhibit a single spectral peak.

Similar to the treatment of the corner modes in Section 4.1, the resonators that host the partial-dislocation induced bound states were appended with loading capacitors to tune their excitations into the spectral range of interest (13.1 MHz - 13.4 MHz). The nominal values of these loading capacitors are listed in Table 4.3 and follow the numbering of the local DOS plots in Fig. 4.5.

Table 4.3: Loading Capacitor Values for Partial Dislocation Plane Defects

Component	**Nominal value**	**Tolerance**
Bulk-terminated partial dislocation		
$C_{1'}$	24 pF	±5%
$C_{2'}$	1 pF	±0.1 pF
Boundary-terminated partial dislocation		
$C_{1''}$	24 pF	±5%
$C_{2''}$	24 pF	±5%

Next, the robustness of these bound states was experimentally investigated by extending the partial dislocation to span the entire 2D material. To achieve this, the partial dislocation defect was extended to form a 4 × 12 unit cell configuration as shown in Fig. 4.5b, where both ends terminate at the boundary. The bound states associated with the defect should be robust irrespective of whether the partial dislocation terminates within the bulk or at the boundary of the TCI, as might be expected since the band structure of the boundary itself is gapped. Experimental measurements confirm that the two bound states now simply relocate to the new higher-order boundaries of the partial dislocation, confirming their robustness. The local DOS of each site in the measured metamaterial is provided in Fig. 4.7, and the spectra of the bound states are highlighted in yellow. It can be observed that the local DOS of the bound states exhibit a single spectral peak, indicating that they are spectrally isolated from the bulk modes in the system.

4.2.2 Partial dislocations in a octupole TCI

This section focuses on partial dislocation defects in 3D octupole TCIs and applies the same methodology used in Section 4.2.1. Similar to the 2D quadrupole TCI experiments, periodic boundary conditions were imposed along the z-direction to eliminate the outer corner modes and to minimize

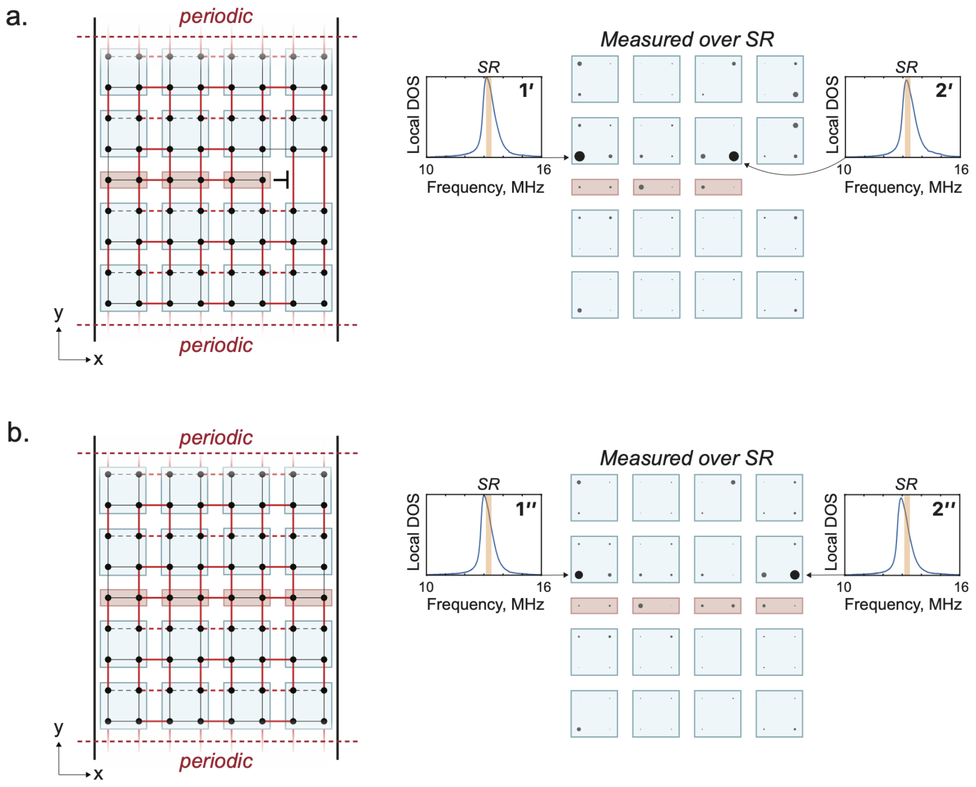

Figure 4.5: Quadrupole TCI partial dislocation experiments. **(a)** Topology of the measured quadrupole TCI with an bulk-terminated partial dislocation and spatial map of the mode density at each site over the spectral range (SR) of 13.1 MHz - 13.4 MHz. The blue boxes represent complete quadrupole unit cells, and the red boxes represent the partial dislocation. The red (black) lines denote strong (weak) coupling, and the dashed lines represent negative coupling. In the spatial map, each site is represented by a circle with radius proportional to the local mode density. The local DOS of the sites with the largest mode densities are shown in the inset and the SR is highlighted in orange. **(b)** Same as (a), but for a boundary-terminated partial dislocation. Complete local DOS measurements for all sites in (a) and (b) are presented in Fig. 4.6 and Fig. 4.7.

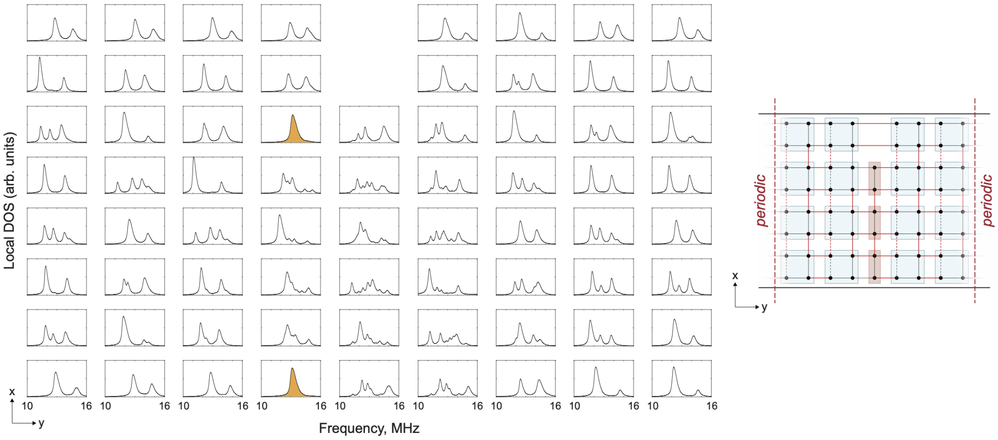

Figure 4.6: Measured local DOS at each site for a 4×4 unit-cell quadrupole TCI with a bulk-terminated partial dislocation. These measurements correspond to Fig. 4.5a. The organization of the grid follows the topology on the right, the red (black) lines denote strong (weak) coupling, and the dashed lines denote negative coupling. In the DOS measurements, sites that are anticipated to host a corner mode or bound state are highlighted in yellow.

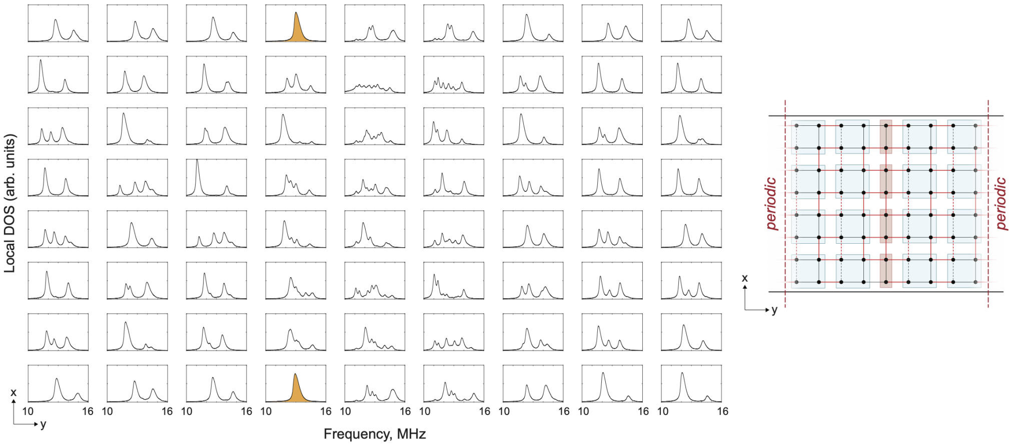

Figure 4.7: Measured local DOS at each site for a 4×4 unit-cell quadrupole TCI with a boundary-terminated partial dislocation. These measurements correspond to Fig. 4.5b. The organization of the grid follows the topology on the right, the red (black) lines denote strong (weak) coupling, and the dashed lines denote negative coupling. In the DOS measurements, sites that are anticipated to host a corner mode or bound state are highlighted in yellow.

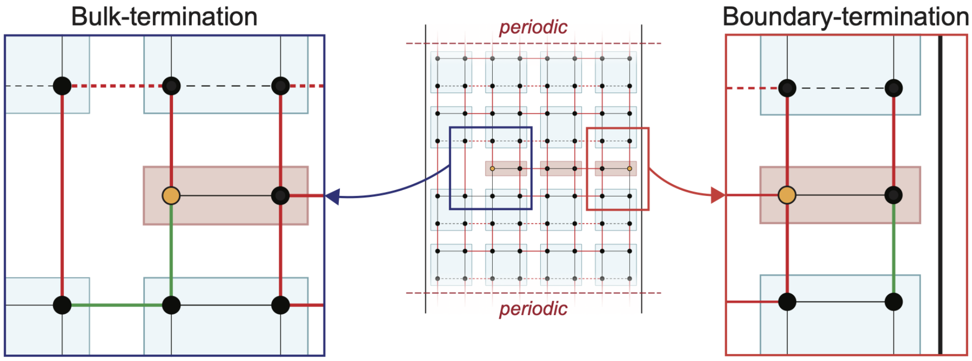

Figure 4.8: Local deformation of coupling to spatially isolate bound states to single sites. Representative examples of how the coupling pattern was locally deformed to spatially isolate the bound states associated with bulk- and boundary-terminated partial dislocation defects to a single site in 2D quadrupole TCIs. The red (black) lines denote strong (weak) coupling, and the dashed lines denote negative coupling. The green lines correspond to where the coupling strength was changed from strong to weak coupling in order to isolate a bound state on the site highlighted in yellow.

boundary effects. This was achieved by physically wiring the top and bottom layers of the octupole TCI together and enabling strong coupling between the two layers using the solder jumpers. A bulk-terminated partial dislocation was then introduced by changing the middle layer of unit cells into a $3 \times 2 \times \frac{1}{2}$ configuration. This was implemented using part of an “A” layer of quadrupole unit cells.

Similar to the quadrupole TCI experiments, the inter-site connectivity at the higher-order boundaries of the partial dislocation was deformed to isolate the topological bound mode to a single site. Details of the local connectivity are presented in Fig. 4.12. In practice, this involved disassembling the 3D array near the partial dislocation defect plane and changing some of the strong coupling connections to weak coupling using the solder jumpers.

Once again, the bound states associated with the partial dislocation could be observed as gapless modes at the higher-order boundaries of the partial dislocation. These results are shown in the spatial map in Fig. 4.9a and in the local DOS measurements in Fig. 4.10. Localized bound states can be observed at the sites directly above the partial dislocation plane. These modes were tuned to appear within a spectrally bare region of the band structure by adding loading capacitors to the resonators that they are spatially localized to. The nominal values of the loading capacitors used to achieve this are listed in Table 4.4. This table follows the numbering of the inset local DOS plots in Fig. 4.9. As before, these results experimentally confirm that the defect-induced bound states survive when the partial dislocation is extended to terminate at the boundary of the material.

Table 4.4: Loading Capacitor Values for Partial Dislocation Plane Defects

Component	**Nominal value**	**Tolerance**
Bulk-terminated partial dislocation		
$C_{1'}$	20 pF	±5%
$C_{2'}$	18 pF	±5%
$C_{3'}$	27 pF	±5%
$C_{4'}$	20 pF	±5%
Boundary-terminated partial dislocation		
$C_{1''}$	20 pF	±5%
$C_{2''}$	24 pF	±5%
$C_{3''}$	27 pF	±5%
$C_{4''}$	20 pF	±5%

Finally, the partial dislocation plane was extended to the outer boundary of the 3D material, using a $3 \times 3 \times \frac{1}{2}$ unit-cell plane. Similar to the bulk-terminated defect, this was implemented using an “A” layer of quadrupole unit cells.

These bound states are again shown to be spectrally gapless and localized to the sites directly above the corners of the partial dislocation plane (Fig. 4.9b and Fig. 4.11). Once again, these modes were tuned to appear within the spectral range of 12.75 MHz - 13.05 MHz by using loading capacitors. The nominal values of these loading capacitors are listed in Table 4.4 and follow the labeling in Fig. 4.9.

This Chapter has provided experimental evidence that 2D quadrupole and 3D octupole TCIs were successfully constructed using the modular circuit-based metamaterial discussed in this thesis. In addition, partial dislocation defects were also constructed and inserted into the multipole lattices. Upon doing so, bound states could be observed near the partial dislocation defect cores and at open material boundaries. These observations support the prediction that partial dislocations should trap bound states in multipole TCIs by effectively creating a spatial phase boundary (Section 2.2). These results highlight the versatility of using a modular approach to construct topological metamaterials.

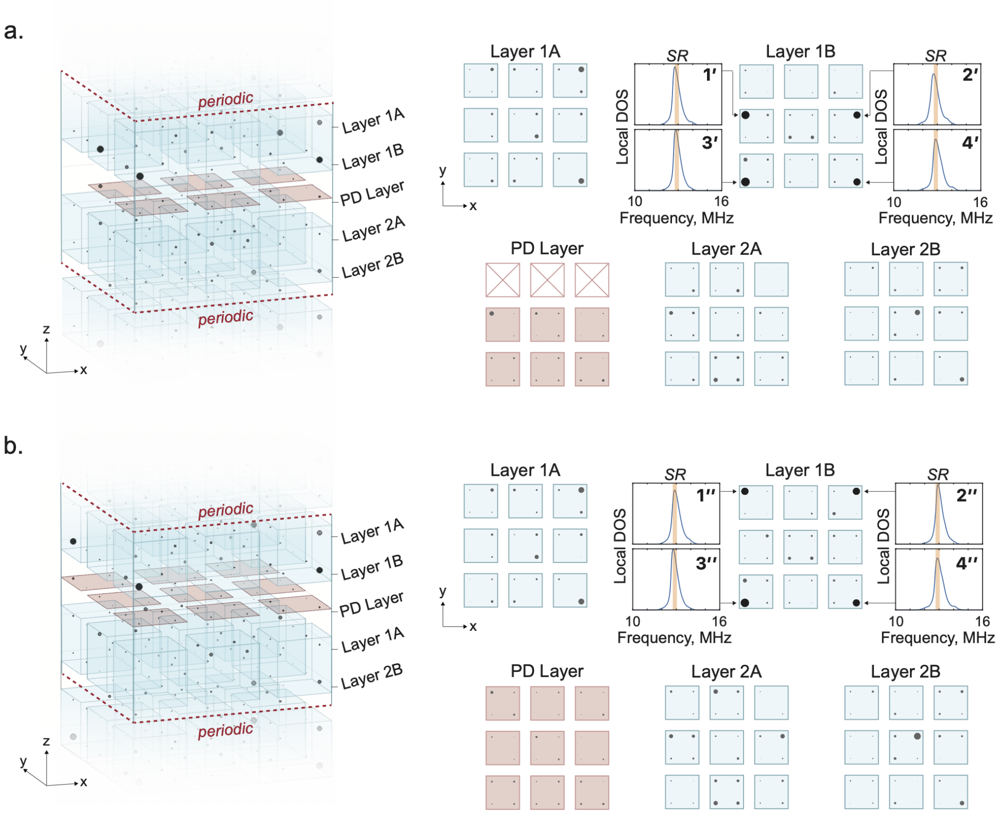

Figure 4.9: Octupole TCI partial dislocation experiments. **(a)** Spatial map of mode density at each site over the spectral range (SR) of 12.75 MHz - 13.05 MHz in an octupole TCI (blue unit cells) with an bulk-terminated partial dislocation (red unit cells). In the spatial map, each site is represented by a circle with radius proportional to the local mode density over the selected SR. The local DOS is shown in the inset for the sites with the largest mode density, and the SR is highlighted in orange. **(b)** same as (a), but for a boundary-terminated partial dislocation. Complete local DOS measurements for all sites in (a) and (b) are presented in Fig. 4.10 and Fig. 4.11.

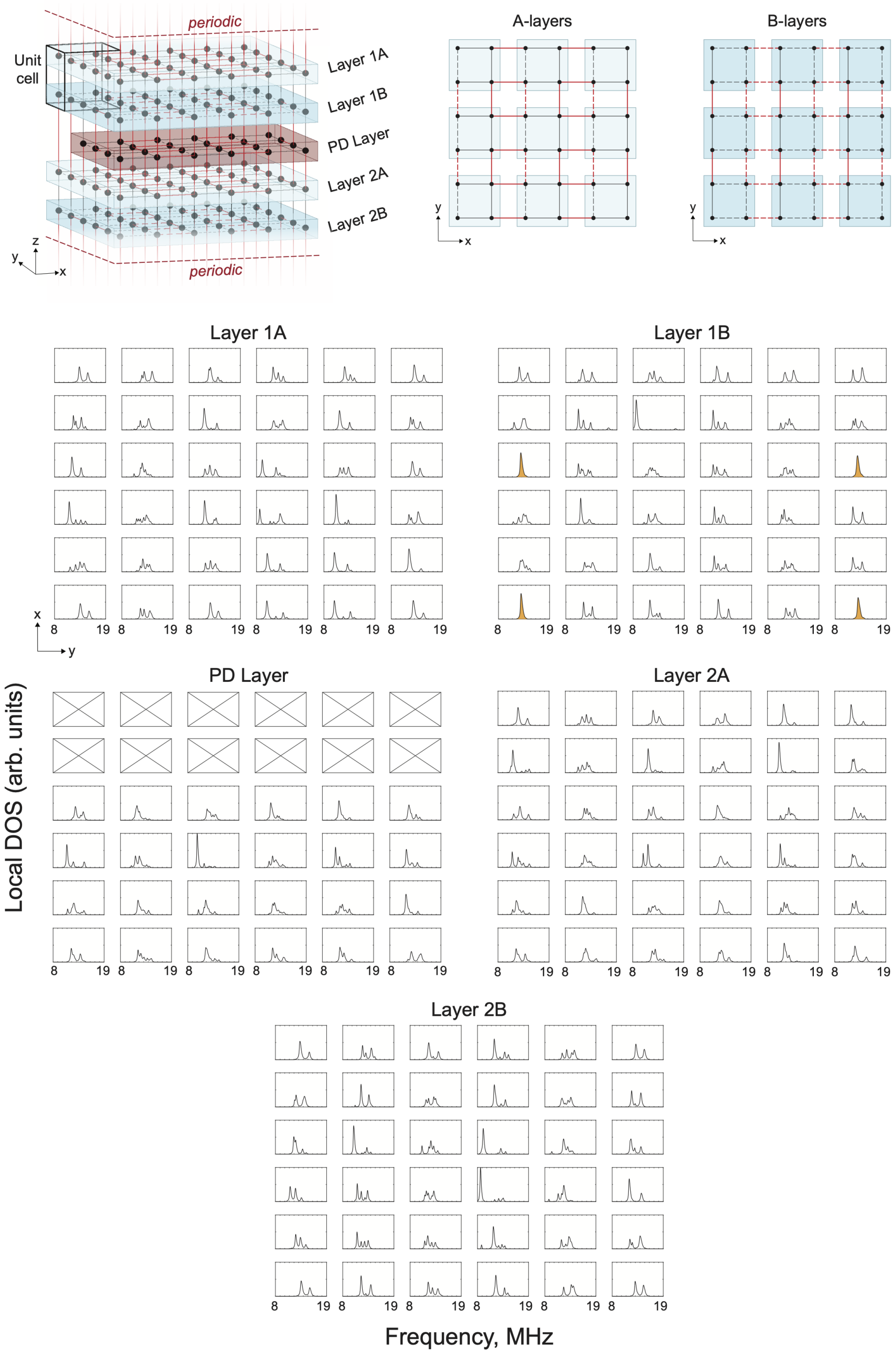

Figure 4.10: Measured local DOS at each site for a $3 \times 3 \times 2$ unit-cell octupole TCI with an bulk-terminated partial dislocation. These measurements correspond to Fig. 4.9a. The defect is realized as 3×2 unit-cell 'A-layer' quadrupole TCI. The organization of the grid follows the topology on the right, the red (black) lines denote strong (weak) coupling, and the dashed lines denote negative coupling. In the DOS measurements, sites that are anticipated to host a corner mode or bound state are highlighted in yellow.

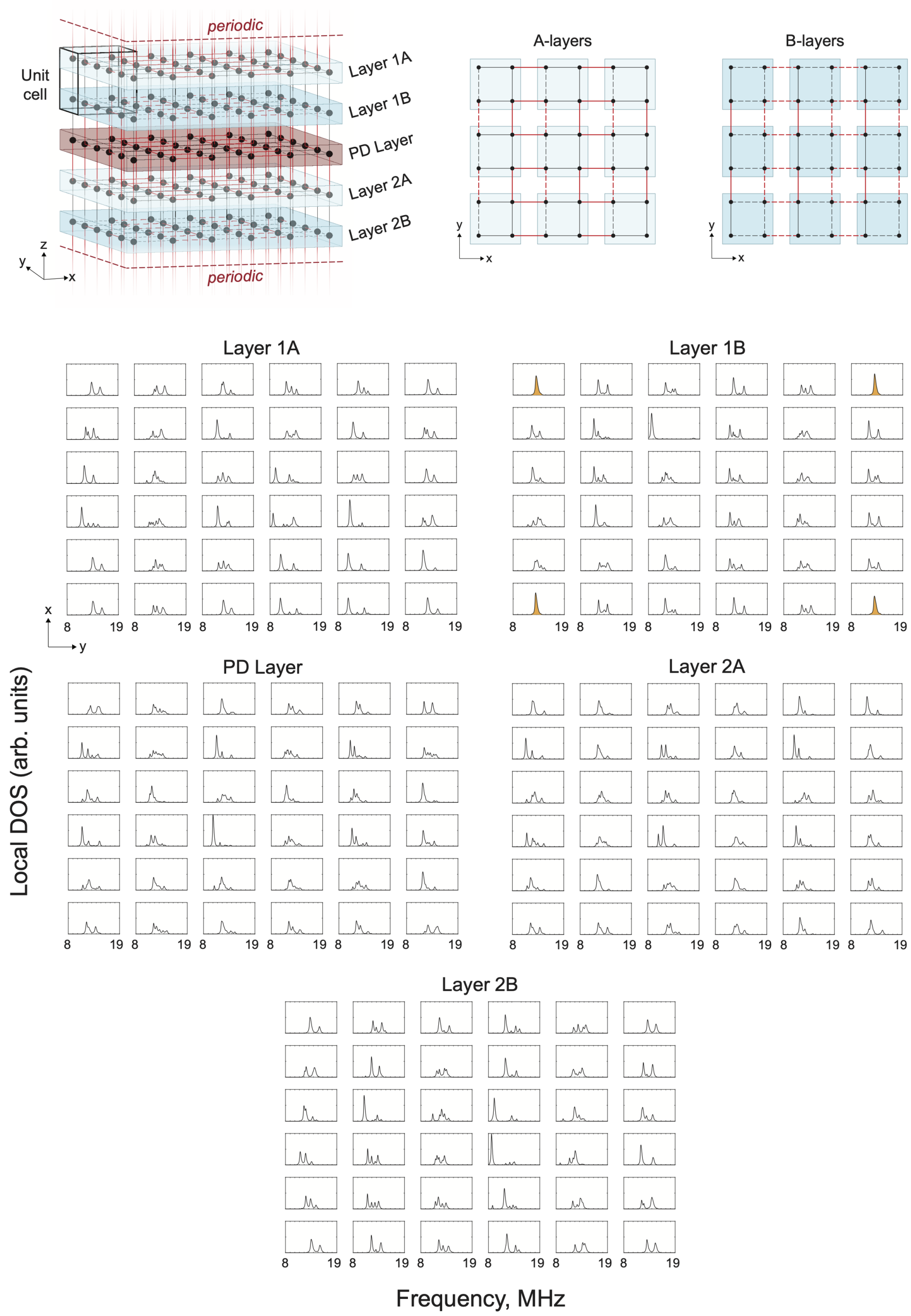

Figure 4.11: Measured local DOS at each site for a $3 \times 3 \times 2$ unit-cell octupole TCI with a boundary-terminated partial dislocation. The defect is realized as an 'A-layer' quadrupole TCI plane. These measurements correspond to Fig. 4.9b. The organization of the grid follows the topology on the right, the red (black) lines denote strong (weak) coupling, and the dashed lines denote negative coupling. In the DOS measurements, sites that are anticipated to host a corner mode or bound state are highlighted in yellow.

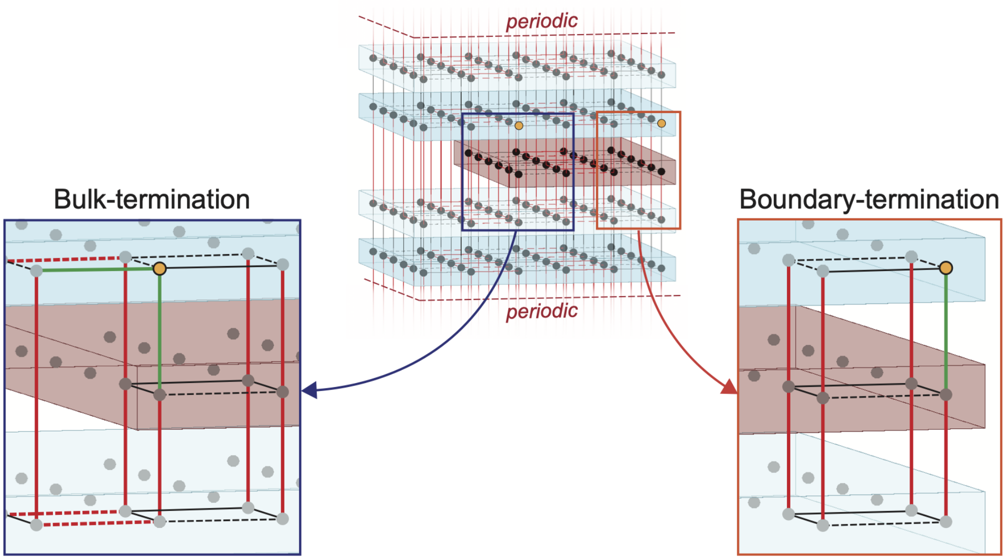

Figure 4.12: Local deformation of coupling to spatially isolate bound states to single sites. Representative examples of how the coupling pattern was locally deformed to spatially isolate the bound states associated with bulk- and boundary-terminated partial dislocation defects to a single site in 3D octupole TCIs. The red (black) lines denote strong (weak) coupling, and the dashed lines denote negative coupling. The green lines correspond to where the coupling strength was changed from strong to weak coupling in order to isolate a bound state on the site highlighted in yellow.

CHAPTER 5

CONCLUSIONS

5.1 Summary of results

In this thesis, partial dislocation defects have been demonstrated to trap bound states in both 2D and 3D multipole HOTIs, which are insensitive to full dislocations. Furthermore, when compared to other crystallographic defects, partial dislocations have the noteworthy property of being able to trap bound states in insulators that have nominally trivial topology. It is anticipated that the bound states trapped by these defects can be harnessed for potential engineering applications, such as topological lasing, as these findings provide a pathway to selectively embed protected states deep within the bulk of both topologically trivial and non-trivial insulators with appropriate sublattice structure and embedded topology. This implies that robust bulk modes can be created by defect networks deep inside even a nominally trivial insulator, where they will be shielded from the ambient environment, and without the concern that they may couple to, and hybridize with, topological modes on the edges/surfaces. One can also envision that implementing these defect networks in a dynamic system, where the coupling between sites is reconfigurable, could produce a device where bound states can be moved throughout the bulk. More broadly, partial dislocation defects are abundant in solid-state materials, and may provide a powerful new probe of topology in quantum materials.

5.2 Suggested future work

The topological insulators discussed in this thesis are all Hermitian systems. Specifically, this means that the Hamiltonian matrix for each of these models is equal to its own conjugate transpose [21] and thus has real energy eigenvalues. To date, most of the work concerning topological insulators has concerned Hermitian models; however, the study of non-Hermitian topology has become increasingly popular because of the unique properties exhibited by these systems that have no Hermitian equivalent [54, 55]. A general difference between Hermitian and non-Hermitian systems is that the latter can have complex energy eigenvalues. This distinction is responsible for the strange physical phenomena that has become characteristic of non-Hermitian systems (e.g., eigenmode coalescence, momentum-dependent localization).

It is perhaps then unsurprising that many condensed matter theorists have begun to consider how non-trivial topology manifests and interacts with a non-Hermitian system [54, 55]. Progress in this field has been rapid, and some theorists are already considering how crystallographic defects interact with these systems [56, 57]. This fast-paced theoretical progress has created many opportunities for experimentalists; however, many of the non-Hermitian models used in these studies cannot be constructed with established coupled-resonator metamaterials. This is due to the passive nature the systems described in Section 3.1.2.

On the other hand, topolectric circuits have proven to be a well-suited experimental platform to realize non-Hermitian topological systems [58, 59, 60]. Compared to acoustic, phononic, and photonic systems, active components are much easier to design into a circuit architecture. This has allowed non-Hermitian systems to be quickly constructed using the topolectric circuit framework. It is then suggested that the topolectric circuit approach be adopted to implement any non-Hermitian systems of interest. As discussed in Section 3.1.2, one of the primary disadvantages of this approach is the number of measurements required to characterize the system (n^2 measurements for a n-site system). To avoid an overly tedious measurement procedure, it is critical that some level of automation is involved. This can be achieved by making use of data acquisition and/or multiplexing equipment with a suitable number of input channels. Special consideration should also be made to ensure that the operating frequency (that the topolectric circuit is evaluated at) is appropriate for the measurement tools. There is some trade-off between lower operating frequencies and the tolerance of the constituent components that should be optimized.

REFERENCES

[1] D. Bisharat, R. Davis, Y. Zhou, P. Bandaru, and D. Sievenpiper, "Photonic topological insulators: A beginner's introduction," *IEEE Antennas and Propagation Magazine*, vol. 63, no. 3, pp. 112–124, 2021.

[2] M. G. Vergniory, L. Elcoro, C. Felser, N. Regnault, B. A. Bernevig, and Z. Wang, "A complete catalogue of high-quality topological materials," *Nature*, vol. 566, no. 7745, pp. 480–485, Feb 2019.

[3] M. Serra-Garcia, V. Peri, R. Süsstrunk, O. R. Bilal, T. Larsen, L. G. Villanueva, and S. D. Huber, "Observation of a phononic quadrupole topological insulator," *Nature*, vol. 555, pp. 342–345, 2018.

[4] Y. Qi, C. Qiu, M. Xiao, H. He, M. Ke, and Z. Liu, "Acoustic realization of quadrupole topological insulators," *Physical Review Letters*, vol. 124, p. 206601, 5 2020.

[5] X. Ni, M. Li, M. Weiner, A. Alù, and A. B. Khanikaev, "Demonstration of a quantized acoustic octupole topological insulator," *Nature Communications*, vol. 11, p. 2108, 12 2020.

[6] H. Xue, Y. Ge, H.-X. Sun, Q. Wang, D. Jia, Y.-J. Guan, S.-Q. Yuan, Y. Chong, and B. Zhang, "Observation of an acoustic octupole topological insulator," *Nature Communications*, vol. 11, p. 2442, 12 2020.

[7] S. Imhof, C. Berger, F. Bayer, J. Brehm, L. W. Molenkamp, T. Kiessling, F. Schindler, C. H. Lee, M. Greiter, T. Neupert, and R. Thomale, "Topolectrical-circuit realization of topological corner modes," *Nature Physics*, vol. 14, pp. 925–929, 2018.

[8] J. Bao, D. Zou, W. Zhang, W. He, H. Sun, and X. Zhang, "Topoelectrical circuit octupole insulator with topologically protected corner states," *Physical Review B*, vol. 100, p. 201406, Nov 2019.

[9] C. W. Peterson, W. A. Benalcazar, T. L. Hughes, and G. Bahl, "A quantized microwave quadrupole insulator with topologically protected corner states," *Nature*, vol. 555, no. 7696, p. 346, 2018.

[10] S. Mittal, V. V. Orre, G. Zhu, M. A. Gorlach, A. Poddubny, and M. Hafezi, “Photonic quadrupole topological phases,” *Nature Photonics*, vol. 13, pp. 692–696, 10 2019.

[11] S. S. Yamada, T. Li, M. Lin, C. W. Peterson, T. L. Hughes, and G. Bahl, “Bound states at partial dislocation defects in multipole higher-order topological insulators,” *arXiv preprint*, p. 2105.01050, 2021.

[12] L. Lu, J. D. Joannopoulos, and M. Soljačić, “Topological photonics,” *Nature Photonics*, vol. 8, no. 11, pp. 821–829, Nov 2014.

[13] “The nobel prize in physics 2016,” Oct 2016. [Online]. Available: https://www.nobelprize.org/prizes/physics/2016/press-release/

[14] “The nobel prize in physics 1985,” Oct 1985. [Online]. Available: https://www.nobelprize.org/prizes/physics/1985/press-release/

[15] Z. Wang, Y. Chong, J. D. Joannopoulos, and M. Soljačić, “Observation of unidirectional backscattering-immune topological electromagnetic states,” *Nature*, vol. 461, no. 7265, pp. 772–775, Oct 2009.

[16] T. Christensen, H. C. Po, J. D. Joannopoulos, and M. Soljačić, “Location and topology of the fundamental gap in photonic crystals,” *arXiv preprint*, p. 2106.10267, 2021.

[17] P. St-Jean, V. Goblot, E. Galopin, A. Lemaître, T. Ozawa, L. Le Gratiet, I. Sagnes, J. Bloch, and A. Amo, “Lasing in topological edge states of a one-dimensional lattice,” *Nature Photonics*, vol. 11, no. 10, pp. 651–656, Oct. 2017.

[18] M. A. Bandres, S. Wittek, G. Harari, M. Parto, J. Ren, M. Segev, D. N. Christodoulides, and M. Khajavikhan, “Topological insulator laser: Experiments,” *Science*, vol. 359, no. 6381, 2018.

[19] W. P. Su, J. R. Schrieffer, and A. J. Heeger, “Solitons in polyacetylene,” *Phys. Rev. Lett.*, vol. 42, pp. 1698–1701, Jun 1979.

[20] J. Asbóth, L. Oroszlány, and A. Pályi, *A Short Course on Topological Insulators: Band Structure and Edge States in One and Two Dimensions*, ser. Lecture Notes in Physics. Springer International Publishing, 2016.

[21] D. J. Griffiths, *Introduction to Quantum Mechanics.* Pearson Prentice Hall, 2005.

[22] H. Watanabe and S. Ono, “Corner charge and bulk multipole moment in periodic systems,” *Physical Review B*, vol. 102, p. 165120, Oct 2020.

[23] S. Ren, I. Souza, and D. Vanderbilt, "Quadrupole moments, edge polarizations, and corner charges in the wannier representation," *Physical Review B*, vol. 103, p. 035147, Jan 2021.

[24] W. A. Benalcazar, B. A. Bernevig, and T. L. Hughes, "Electric multipole moments, topological multipole moment pumping, and chiral hinge states in crystalline insulators," *Physical Review B*, vol. 96, p. 245115, Dec 2017.

[25] W. A. Benalcazar, B. A. Bernevig, and T. L. Hughes, "Quantized electric multipole insulators," *Science*, vol. 357, no. 6346, pp. 61–66, 2017.

[26] M. Fruchart and V. Vitelli, "Waves cornered," Mar 2018. [Online]. Available: https://www.nature.com/articles/d41586-018-02868-4?WT.ec_id=NATURE-20180316&spMailingID=56197970&spUserID=MjA1NzcwMjE4MQS2&spJobID=1362348899&spReportId=MTM2MjM0ODg5OQS2

[27] I. H. Grinberg, M. Lin, W. A. Benalcazar, T. L. Hughes, and G. Bahl, "Trapped state at a dislocation in a weak magnetomechanical topological insulator," *Physical Review Applied*, vol. 14, 12 2020.

[28] C. W. Peterson, T. Li, W. Jiang, T. L. Hughes, and G. Bahl, "Trapped fractional charges at bulk defects in topological insulators," *Nature*, vol. 589, pp. 376–380, 1 2021.

[29] Y. Liu, S. Leung, F. F. Li, Z. K. Lin, X. Tao, Y. Poo, and J. H. Jiang, "Bulk–disclination correspondence in topological crystalline insulators," *Nature*, vol. 589, pp. 381–385, 1 2021.

[30] G. Harari, M. A. Bandres, Y. Lumer, M. C. Rechtsman, Y. D. Chong, M. Khajavikhan, D. N. Christodoulides, and M. Segev, "Topological insulator laser: Theory," *Science*, vol. 359, no. 6381, 2018.

[31] Y. Ran, Y. Zhang, and A. Vishwanath, "One-dimensional topologically protected modes in topological insulators with lattice dislocations," *Nature Physics*, vol. 5, no. 4, p. 298, 2009.

[32] F.-F. Li, H.-X. Wang, Z. Xiong, Q. Lou, P. Chen, R.-X. Wu, Y. Poo, J.-H. Jiang, and S. John, "Topological light-trapping on a dislocation," *Nature Communications*, vol. 9, no. 1, p. 2462, 2018.

[33] R. Noguchi, T. Takahashi, K. Kuroda, M. Ochi, T. Shirasawa, M. Sakano, C. Bareille, M. Nakayama, M. Watson, K. Yaji et al., "A weak topological insulator state in quasi-one-dimensional bismuth iodide," *Nature*, vol. 566, no. 7745, p. 518, 2019.

[34] J. C. Teo and C. L. Kane, "Topological defects and gapless modes in insulators and superconductors," *Physical Review B*, vol. 82, no. 11, p. 115120, 2010.

[35] V. Juričić, A. Mesaros, R.-J. Slager, and J. Zaanen, "Universal probes of two-dimensional topological insulators: dislocation and π flux," *Physical Review Letters*, vol. 108, no. 10, p. 106403, 2012.

[36] R.-J. Slager, A. Mesaros, V. Juričić, and J. Zaanen, "Interplay between electronic topology and crystal symmetry: Dislocation-line modes in topological band insulators," *Physical Review B*, vol. 90, no. 24, p. 241403, 2014.

[37] J. C. Teo and T. L. Hughes, "Topological defects in symmetry-protected topological phases," *Annual Review of Condensed Matter Physics*, vol. 8, pp. 211–237, 2017.

[38] W. A. Benalcazar, T. Li, and T. L. Hughes, "Quantization of fractional corner charge in C_n-symmetric higher-order topological crystalline insulators," *Physical Review B*, vol. 99, p. 245151, Jun 2019.

[39] C. W. Peterson, T. Li, W. A. Benalcazar, T. L. Hughes, and G. Bahl, "A fractional corner anomaly reveals higher-order topology," *Science*, vol. 369, no. 6495, p. 1114, 2020.

[40] B. Bradlyn, L. Elcoro, J. Cano, M. G. Vergniory, Z. Wang, C. Felser, M. I. Aroyo, and B. A. Bernevig, "Topological quantum chemistry," *Nature*, vol. 547, no. 7663, pp. 298–305, Jul 2017.

[41] T. Li, P. Zhu, W. A. Benalcazar, and T. L. Hughes, "Fractional disclination charge in two-dimensional C_n-symmetric topological crystalline insulators," *Physical Review B*, vol. 101, p. 115115, Mar 2020.

[42] W. A. Benalcazar, J. C. Teo, and T. L. Hughes, "Classification of two-dimensional topological crystalline superconductors and majorana bound states at disclinations," *Physical Review B*, vol. 89, no. 22, p. 224503, 2014.

[43] M. Geier, I. C. Fulga, and A. Lau, "Bulk-boundary-defect correspondence at disclinations in rotation-symmetric topological insulators and superconductors," *SciPost Physics*, vol. 10, p. 92, 2021.

[44] Q. Wang, H. Xue, B. Zhang, and Y. D. Chong, "Observation of protected photonic edge states induced by real-space topological lattice defects," *Physical Review Letters*, vol. 124, p. 243602, Jun 2020.

[45] R. Queiroz, I. C. Fulga, N. Avraham, H. Beidenkopf, and J. Cano, "Partial lattice defects in higher-order topological insulators," *Physical Review Letters*, vol. 123, no. 26, p. 266802, 2019.

[46] G. Van Miert and C. Ortix, "Dislocation charges reveal two-dimensional topological crystalline invariants," *Physical Review B*, vol. 97, no. 20, p. 201111, 2018.

[47] R.-J. Slager, "The translational side of topological band insulators," *Journal of Physics and Chemistry of Solids*, vol. 128, pp. 24–38, 2019.

[48] A. K. Nayak, J. Reiner, R. Queiroz, H. Fu, C. Shekhar, B. Yan, C. Felser, N. Avraham, and H. Beidenkopf, "Resolving the topological classification of bismuth with topological defects," *Science Advances*, vol. 5, no. 11, p. eaax6996, 2019.

[49] B. Roy and V. Juričić, "Dislocation as a bulk probe of higher-order topological insulators," *Phys. Rev. Research*, vol. 3, p. 033107, Jul 2021.

[50] T. I. Tuegel, V. Chua, and T. L. Hughes, "Embedded topological insulators," *Physical Review B*, vol. 100, no. 11, p. 115126, 2019.

[51] C. H. Lee, S. Imhof, C. Berger, F. Bayer, J. Brehm, L. W. Molenkamp, T. Kiessling, and R. Thomale, "Topolectrical circuits," *Communications Physics*, vol. 1, no. 1, p. 39, Jul 2018.

[52] J. Dong, V. Juričić, and B. Roy, "Topolectric circuits: Theory and construction," *Phys. Rev. Research*, vol. 3, p. 023056, Apr 2021. [Online]. Available: https://link.aps.org/doi/10.1103/PhysRevResearch.3.023056

[53] D. M. Pozar, *Microwave engineering; 3rd ed.* Hoboken, NJ: Wiley, 2005.

[54] H. Shen, B. Zhen, and L. Fu, "Topological band theory for non-hermitian hamiltonians," *Phys. Rev. Lett.*, vol. 120, p. 146402, Apr 2018. [Online]. Available: https://link.aps.org/doi/10.1103/PhysRevLett.120.146402

[55] Z. Gong, Y. Ashida, K. Kawabata, K. Takasan, S. Higashikawa, and M. Ueda, "Topological phases of non-hermitian systems," *Phys. Rev. X*, vol. 8, p. 031079, Sep 2018.

[56] C.-H. Liu and S. Chen, "Topological classification of defects in non-hermitian systems," *Phys. Rev. B*, vol. 100, p. 144106, Oct 2019. [Online]. Available: https://link.aps.org/doi/10.1103/PhysRevB.100.144106

[57] X.-Q. Sun, P. Zhu, and T. L. Hughes, "Geometric response and disclination-induced skin effects in non-hermitian systems," *Phys. Rev. Lett.*, vol. 127, p. 066401, Aug 2021. [Online]. Available: https://link.aps.org/doi/10.1103/PhysRevLett.127.066401

[58] T. Hofmann, T. Helbig, F. Schindler, N. Salgo, M. Brzezińska, M. Greiter, T. Kiessling, D. Wolf, A. Vollhardt, A. Kabaši, C. H. Lee, A. Bilušić, R. Thomale, and T. Neupert, "Reciprocal skin effect and its realization in a topolectrical circuit," *Phys. Rev. Research*, vol. 2, p. 023265, Jun 2020.

[59] T. Helbig, T. Hofmann, S. Imhof, M. Abdelghany, T. Kiessling, L. W. Molenkamp, C. H. Lee, A. Szameit, M. Greiter, and R. Thomale, "Generalized bulk–boundary correspondence in non-hermitian topolectrical circuits," *Nature Physics*, vol. 16, no. 7, pp. 747–750, Jul 2020.

[60] S. Liu, R. Shao, S. Ma, L. Zhang, O. You, H. Wu, Y. J. Xiang, T. J. Cui, and S. Zhang, "Non-hermitian skin effect in a non-hermitian electrical circuit," *Research*, vol. 2021, p. 5608038, Mar 2021.